UNIVERSITY OF TWENTE.

Physics of Fluids

Master thesis
Erik Christian Linnartz

Contrast agents for continuous wave photoacoustics

Committee
Ir. Guillaume Lajoinie M.Sc.
prof. Michel Versluis
Dr. Jeroen Verschuur
prof. Devaraj van der Meer
prof. Nico de Jong

July 4th, 2014

Abstract

Photoacoustic imaging is a widely investigated imaging method that allows for clear differentiation between different tissues (specificity). Contrast bubble enhanced ultrasound imaging is already used a lot and despite less specificity, the bubbles create great contrast. In this report we investigate the possibilities of using contrast bubbles in combination with photoacoustics in order to combine the advantages of both methods.

Contrast agents are investigated for photoacoustic imaging with a continuous wave laser. We show that polymeric microcapsules, that proved to be an effective contrast agent for pulsed laser photoacoustics, also work with a modulated continuous wave laser but require a high laser power. Oil coated microbubbles are suggested as a new contrast agent for continuous wave photoacoustics and numerical simulations are performed to find out what the optimal parameters and material properties for this contrast agent would be. A simplified model provides physical understanding of the simulated results. We also show current work in the process towards producing these contrast agents in micro-fluidic devices.

Contents

Chapter 1

Introduction

As practitioner of integrative medicine Chris Kresser said *"In medicine, the key to choosing the best treatment is an accurate diagnosis. If the diagnosis isn't correct, the treatment will be ineffective – or even cause harm."* [1] Imaging of the human body is often, especially in case of cancer a key method for early and accurate diagnosis. But in a world where, according to the Centers for Disease Control and Prevention, the leading causes of death are heart disease and cancer [2], improving imaging of the human body is one of the most important challenges of this time [3].

Several different methods for imaging have been developed such as ultrasound imaging (US), magnetic resonance imaging (MRI), optical coherence microscopy (OCT), X-ray and X-ray computed tomography (CT), nuclear imaging techniques like positron emission tomography (PET) and single photon emission computed tomography (SPECT) and photoacoustic imaging (PAI). All imaging methods have their own advantages in terms of resolution, contrast, penetration depth, cost and other aspects [4]. This master thesis will be about photoacoustic imaging (PAI).

PAI works by sending light into a body. Depending on the materials it encounters, a certain amount of light is absorbed, the material heats up and therefore it expands. This expansion gives a pressure wave which is by definition sound. PAI is thus a hybrid technology where light is send but sound is received and can be measured with the standard ultrasound equipment.

PAI has a high contrast, sub-millimeter scale resolution and reasonable penetration depth (up to several cm) [4]. However, the main advantage of PAI is that it has a high specificity: One can clearly differentiate the signal of different materials or tissues. Ultrasound imaging on the other hand, has less specificity but contrast agent enhanced ultrasound imaging produces great contrast due to the acoustic resonance of bubbles. In this report we investigate the possibilities of using contrast bubbles in combination with photoacoustics in order to combine the advantages of both methods.

In case of PAI, contrast agents give a high photoacoustic signal and are therefore very visible on the image. Contrast agents can be used to image arteries and diffusion of contrast-agent-sized particles like red blood cells. Also, by making a contrast agent that prefers to stick to a specific molecule or organ, organs and the presence of specific molecules can be visualized [5]. These contrast agents, which are usually coated bubbles or capsules, can also be carrying drugs thereby facilitating targeted drug delivery and making these bubbles oscillate can have a mechanical influence in the body [6]. Earlier research at the Physics of Fluids group has shown that monodispersed microcapsules are a good contrast agents [7] and these will also be used in the first chapter of this thesis.

Photoacoustics started when Alexander Graham Bell described producing sound by light in 1880 [8]. For a long time this effect was not used very much but the invention of the laser in the 1970s meant the start of quick development of PAI [7]. Currently there are already some commercialized preclinical PAI applications and in order to make PAI widely used and a significant contributor to early diagnosis, some improvements are still required [9]. One issue of most PAI devices is the requirement of high energy pulsed lasers, these are expensive and often big. Modulated continuous wave diode lasers have been proposed [10, 11] but these don't have very high power limiting the ultrasound signal that is received. In this thesis solid state pumped continuous wave lasers modulated with an acousto optic modulator are used instead. This combination can result in a system that has higher power than diode lasers but is cheaper and smaller than pulsed lasers.

1.1 Thesis outline

In the first following chapter (chapter 2), we push further the study of an already known potential contrast agents for photoacoustic imaging. The agent consists of polymeric microcapsules filled with hexadecane oil. This chapter aims at demonstrating their applicability for high frequency modulated CW laser photoacoustics. It turns out that relatively high laser powers are required. The third chapter aims at finding an alternative to these capsules. In chapter three, numerical simulations are done to predict the response of oil-coated microbubbles with dye in the oil layer. From this the parameters of the optimal bubble parameters can be extracted. Also presented in this chapter is a simplified theoretical model which is used to make much faster simulations and a linearization of this simplified model to gain understanding of what the simulation predicts. The final chapter describes the latest results in our attempts to create these oil-coated bubbles. Here, our achievements as well as the main difficulties encountered in the process are described.

Chapter 2

Continuous wave photoacoustic response from polymeric microcapsules activated by high frequency laser modulation.

This chapter investigates the use of polymeric microcapsules as a photoacoustic contrast agent for a setup with a solid state pumped continuous wave (CW) laser in combination with an acousto optic modulator. These capsules have been used before in combination with a pulsed laser but the mechanisms for such a system are very different and a CW laser is often cheaper and less bulky than a pulsed laser.

In the experiment, the laser is initially set to shine continuously on a capsule. The dye containing polymer shell absorbs the laser light and heats up until the polymer reaches its melting temperature and the capsule breaks. At this moment, the water is already above boiling temperature but the 280 °C oil flow is required to create a vapor nucleus. This process takes less than one millisecond and after this the laser is modulated as a sine wave. The capsule shell heats up during high laser powers, this instantly heats up the bubble that expands. The gas then cools down during low laser powers causing the bubble to shrink. This expanding and shrinking of the bubble goes with high speeds producing a pressure wave propagating in the water which is measured with an ultrasound transducer. At the same time, the capsule response is optically recorded with a high speed video camera. The exact mechanism of bubble nucleation is discussed in Lajoinie's thesis [7].

2.1 Methods and materials

The experimental setup is shown in Figure 2.1. In this setup a 2.55 W, 532 nm, TEM00 CW laser is used (Changchun New Industries Optoelectronics Tech. Co. Ltd.). The AOM used is the MQ180-AO,25-VIS from AA opto-acoustics. Several different high speed cameras of the company Photron have been used: The FASTCAM SA-X2 type 1080K-M4, FASTCAM SA-X type 324K-M4 and the FASTCAM SA2 model 86K-C2. A Panametrics C302-S (Olympus-NDT) focused ultrasound transducer with a diameter of 1 inch (25.4 mm), a center frequency of 1 MHz and focal distance of 1.63 inch (41.4 mm) was connected to a Panametrics amplifier model 5077PR which in turn was connected to a Tektronix Model DPO4034 oscilloscope. The light source used was a Schott KL 2500 LED. A water immersed 60× Olympus objective was used for the microscope and the capsules were contained in an Opticell$^{\mathrm{TM}}$.

2.1.1 Alignment

For the experimental setup, the laser was aligned through the AOM, microscope and focusing lenses. In Figure 2.1 the full setup can be seen. A CW laser shines through a lens with a focal distance of 750 mm in order to have the desired beam waist width in the focal point. The AOM is placed in this focal point and two adjustable mirrors are used to guide where the laser hits the AOM (one mirror required) and under which angle the beam hits the AOM (two mirrors required). It is important that the laser light polarization is in line with the requirements for the AOM. In our case this meant that the laser had to be tilted sideways approximately 60 degrees and for accuracy the tilt of the AOM could be adjusted to get the optimal response. The AOM could also be turned to find the Bragg angle. After the AOM, two more mirrors were placed to again direct the laser beam (not shown in Figure 2.1). The laser then goes through a beam expander which is continuously (i.e. no steps) adjustable between a diverging or converging beam to control the laser spot size. The laser then passes through the microscope objective through which a video recording is also made and the laser spot is aimed at the center of the image. When the video recording is in focus, the spot size of the laser is set.

Now with the laser spot in position, the ultrasound transducer should be coaligned. To achieve this a hydrophone in placed at the location of the sample and brought in focus of the camera by using the 3D translation stage for the sample. Next, the transducer which normally only acts as a receiver, is set to send an ultrasound signal which is recorded by the hydrophone. The focal distance of the transducer (1.63 inch) and the speed of sound in water ($1497\,\mathrm{m s^{-1}}$) are known giving the expected delay before the transmitted ultrasound pulse arrives at the hydrophone ($\approx 27\,\mu\mathrm{s}$). By triggering the oscilloscope this delay can be measured. When a 1 MHz signal is sent with

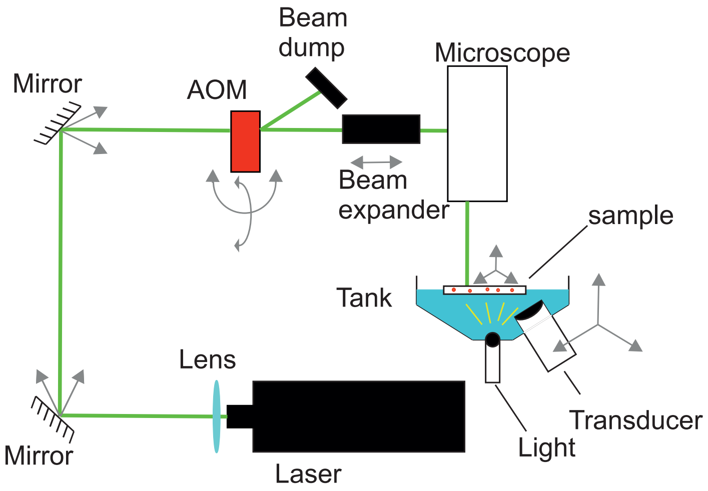

Figure 2.1: The full setup. All grey arrows indicate how all parts can be moved to align the setup.

ten periods (i.e. ten full sine waves) and this is done 200 times per second, the delay time and hydrophone response can be measured 'continuously'. When this is set up, the whole water tank including the transducer can be moved in 3 dimensions and this will be done such that the transducer aims at the hydrophone and the delay is set for the expected delay for a transducer in focus. This way, the transducer will be close to focus but not exactly. By moving the tank in the three dimensions until the ultrasound signal measured by the hydrophone has the maximum amplitude, the best focus can be found.

The result is that the transducer is in focus at the focus of the microscope. This is also where the laser was focused at. The water tank is now fixed and, the hydrophone is replaced by the sample and the sample is brought in focus with the 3D translation stage for the sample.

2.1.2 Capsules

The contrast agents used for this experiment are spherical capsules with a diameter of 6 µm and a poly(methyl methacrylate) (PMMA) polymer shell of 0.6 µm thick. The capsules are filled with hexadecane and the polymer was made with 5 % (weight) Sudan Red 7B dye (Sigma Aldrich). They are made by the company Nanomi with a microsieve$^{\mathrm{TM}}$ emulsification technique.

2.1.3 Bubble detection

Frames of a typical high-speed recording are shown in Figure 2.2. On the left side, the upper frame shows the capsule just before laser irradiation, the middle frame shows a capsule that has a bubble inside and the lower frame

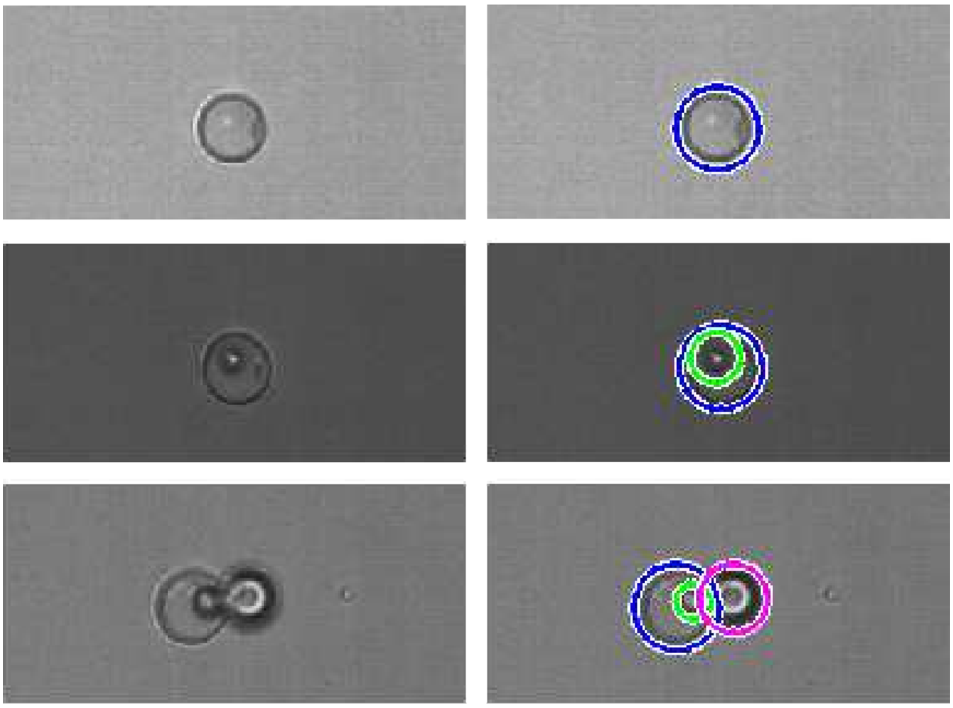

(a) High speed recording (b) Tracking capsule and bubble

Figure 2.2: Bubble tracking

shows a ruptured capsule with a bubble next to it. In order to extract the bubble radius of the many thousands of recorded frames a simple script has been written with Matlab. The script detects the circles with a standard function `imfindcircles` and the rest of the program finds out which circles are the bubble. This is done by assuming the bubble does not change size or location very much between two frames, the bubble is expected outside of the capsule and if concentric circles are found the outer circle considered the full bubble. For example, in the lower left frame in Figure 2.2 the program would detect the bubble and a circle inside the bubble in which case the bigger circle would be chosen as the real bubble. Example results are presented on the right side of Figure 2.2. In these pictures the blue circle is the capsule, the green circle is a bubble inside the capsule and the pink circle is the bubble next to the capsule. The output of the Matlab program is a curve for the radius versus frame number (Figure 2.3) and a movie showing the tracked bubble. Because the frame rate is much lower than the frequency of the laser modulation, the bubble shown in each frame is considered to have the average radius.

Next to measuring the bubble size, the radiated pressure is detected. A typical trace is shown in Figure 2.5 on which it can be seen that the

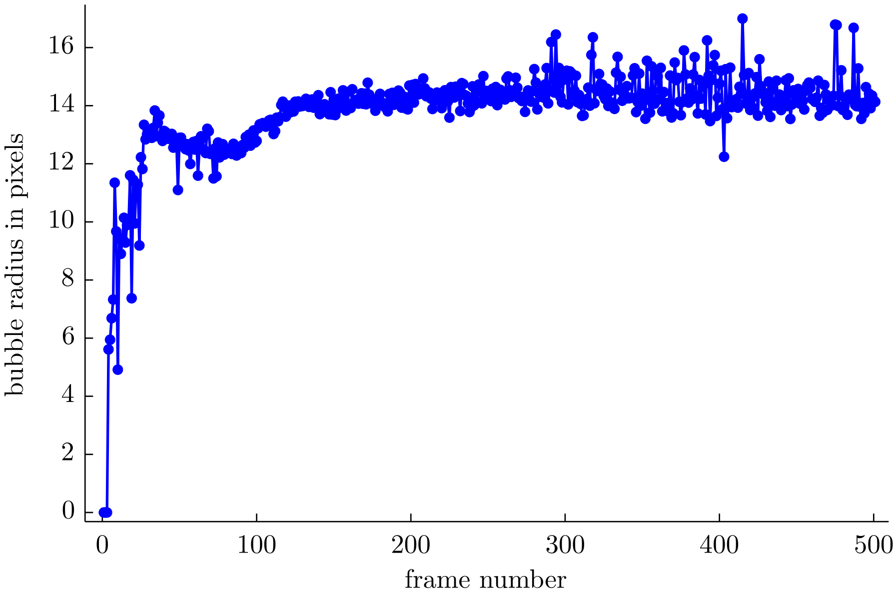

Figure 2.3: Example radius time curve automatic output

radiated pressure has the same frequency as the modulation of the laser with an (expected) phase difference. In order to make the response quantitative the fast Fourier transform (FFT) of the signal is computed as shown in Figure 2.4. This figure shows a clear peak exactly at the driving frequency of 1.2 MHz. The height of this peak is a measure for the radiated pressure.

2.1.4 Results

The bubble radius and the FFT amplitude at the expected frequency are combined to give resonance curves as shown in Figures 2.6 and 2.7. Figure 2.6 shows the response at 1 MHz laser modulation and Figure 2.7 shows the response at 700 kHz laser modulation. The error bars show the standard deviation of the bubble size during the recorded frames of the measurement. Next to the data, a Gaussian curve is also drawn to guide the eye. In Figure 2.6 a Gaussian curve is drawn at the diameter corresponding to the Minnaert frequency (6.6 µm). There also seems to be a response at half this diameter (3.3 µm). The data is taken exclusively from bubbles next to a capsule (as in the bottom left picture in Figure 2.2) and free bubbles. The Minnaert frequency as the resonant peak therefore is not unlikely. For the data at 700 kHz (Figure 2.7) the resonant diameter is 9.4 µm. This did not give a good fit and therefore a Gaussian curve is drawn as the best fit instead. Maybe the Minnaert frequency is not how this response should be interpreted. It is for example possible that the vaporization of the water

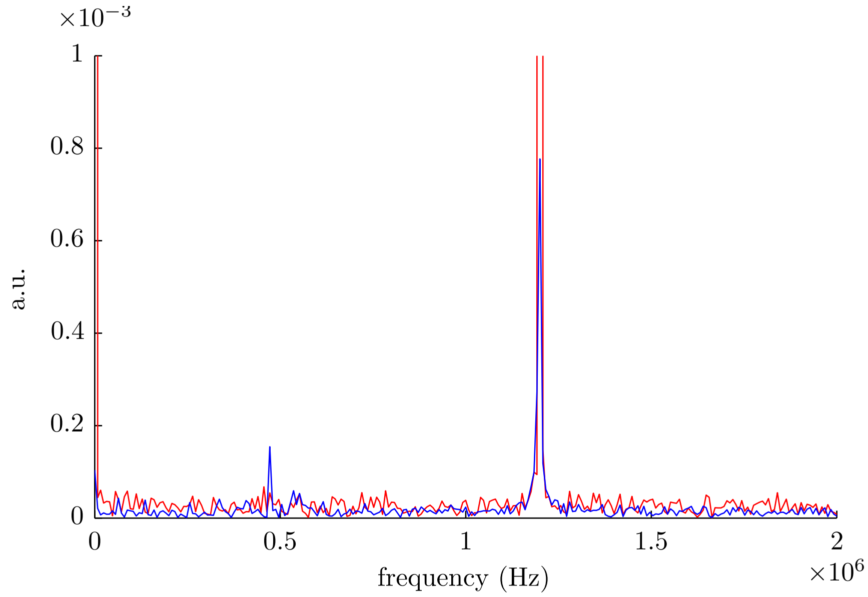

Figure 2.4: The Fourier transform of the oscilloscope trace. The blue line is from the measured ultrasound signal and the red line is from the send to the AOM.

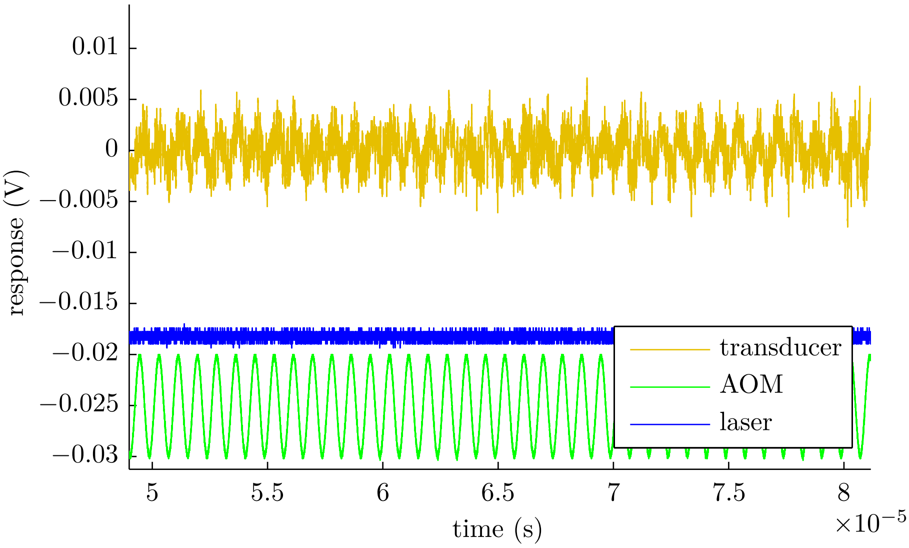

Figure 2.5: Scope trace: The yelow line is the amplified oscilloscope signal and the blue and green line are for the acousto-optic modulator and the laser respectively. The y-axis is only valid for the scope signal and the other signals are adjusted to fit in the same axis.

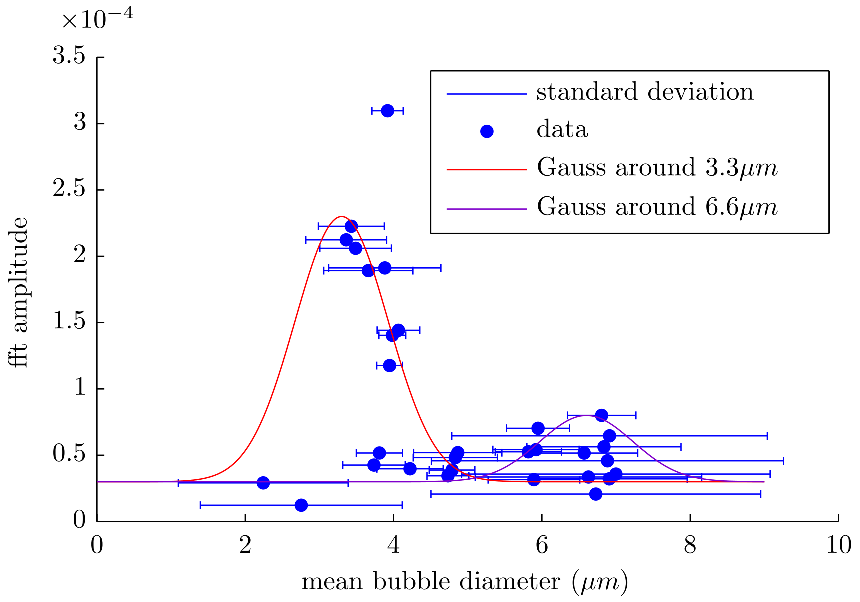

Figure 2.6: Measurement data for for a laser modulated at 1 MHz. The errorbars indicate the standard deviation of the detected bubble size during the video recording used for the data point. The two Gaussian curves are just to guide the eye.

during laser irradiation plays a significant role because of which the bubble cannot be considered a simple free gas bubble.

2.2 Discussion

The data shown in Figures 2.6 and 2.7 demonstrate a bubble diameter dependent response to modulated laser irradiation. However, is not convincing enough to prove the shape of the resonance curve. The accuracy is too low and next to that, the results are not very reproducible. Things that could potentially improve the results are the following:

The used laser was very unreliable. It is supposed to generate a TEM00 beam but often the beam turned into a TEM01 shape. This greatly reduces the power the laser produces and as a result, most of the capsules stayed intact during irradiation. Using a better laser would give more reliable results and would make data gathering quicker.

Another issue is the laser spot which was bigger, but not very much bigger than the capsules. This means that the intensity of irradiation was not perfectly homogeneous which could have had influence on the result. When less laser power would be needed or a more powerful laser is used, a bigger laser spot can be chosen to make sure there is no influence of this

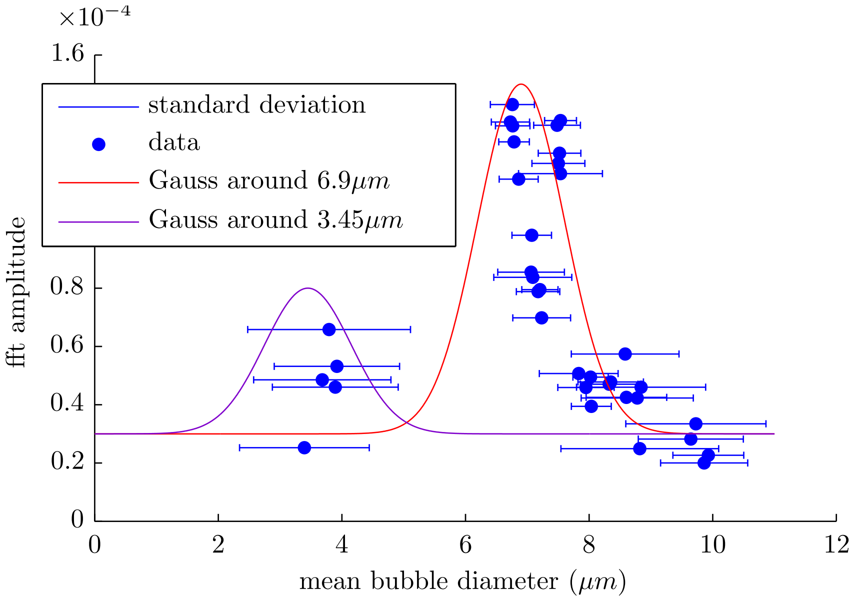

Figure 2.7: Measurement data for 700 kHz Measurement data for for a laser modulated at 700 kHz. The errorbars indicate the standard deviation of the detected bubble size during the video recording used for the data point. The two Gaussian curves are just to guide the eye.

kind.

The high speed camera used in combination with the light source was not optimal. The shutter time could not be set short enough to get rid of motion blur of the oscillating bubble. With the current shutter speed, bubble oscillations were not visible at all because the laser modulation went through several modulations while the shutter is open ($1/f \ll$ shutter time). The solution to this problem would be to use the Brandaris camera which can record up to 25 million frames per second. Another problem related to this is that the light intensity was very low with this shutter speed giving little contrast and much noise. Possibly a more focused or brighter light source can be used.

The capsules don't always respond the same way. The bubble size, shape and the location with respect to the capsule are different every time. Next to this, movement of the capsule could occur making the response even more unique. This unique behavior greatly reduced the reproducibility of the measurement. One solution would be to use higher laser powers to make sure the capsule would shatter completely every time instead of only rupturing at the weakest spot which could be different every time. Another solution would be to use a phospholipid coated bubble that stays intact during irradiation but that can oscillate without breaking the coating. This solution will be described in the following chapters.

Chapter 3

Light absorbing microbubble for low energy contrast enhanced continuous wave photoacoustics

In the previous chapter single polymeric capsules were irradiated by a modulated CW laser in order to generate a CW photoacoustic response. Although these capsule produced an acoustic response, the results were not very reproducible and a relatively high laser power was needed. In this chapter the possibility for a better contrast agent is investigated. In ultrasound imaging many different contrast agents have been used and commercialized. These contrast agents are mostly bubbles which are echogenic due to acoustic resonance. In 1968 it was found that agitated saline functioned as a good US contrast agent due to the echoes of small gas bubbles [12]. Later, contrast agents were stabilized with surfactants, lipids, proteins, polymers or a combination of those [5]. Many of the latest commercialized US contrast agents are coated with phospholipids [6]. In photoacoustics a normal bubble would not function as a good contrast agent because gas does not absorb light efficiently, therefore, for a photoacoustic contrast agent a dye must be added as was the case in the polymer shell of the capsules used in the first chapter of this thesis. Fortunately, much research has been done on adding drugs to US contrast agents and similar methods can be used to add dye instead of drugs to these bubbles. Unger et al. shows five different methods to put drugs in a phospholipid coated microbubble [13], these include: Attaching the drugs to the coating, incorporating the drugs in the coating, non-covalent bounding of drug containing materials (e.g. DNA) and the interior of the bubble can be loaded with drugs incorporated in a oil film that surrounds the microbubble. In all these cases the drugs can be replaced by a dye to make bubbles that heat up during irradiation. It can be expected that the

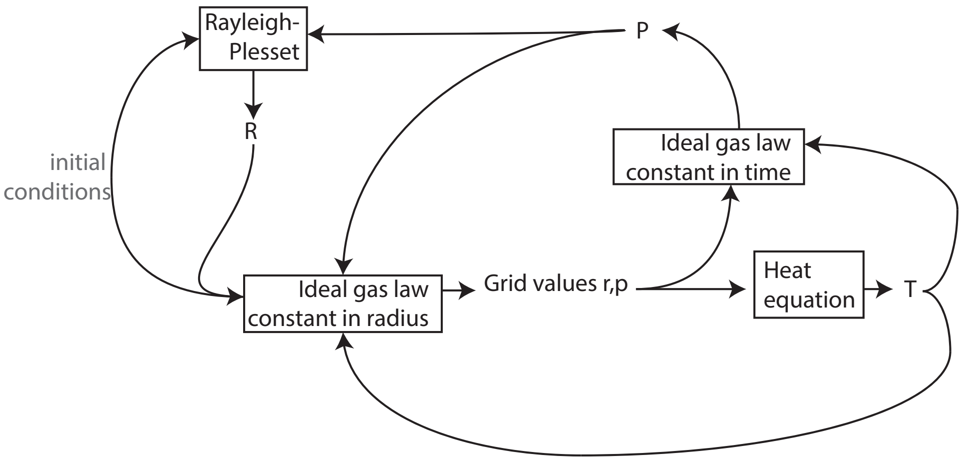

Figure 3.1: The grid used for the simulations

oil layer would be able to hold most dye and therefore would produce the best photoacoustic contrast agent.

Instead of a hard capsule that needs to break in order to produce a bubble, a bubble with a flexible coating is investigated. This way, a nucleation site already exists and much of the initial energy to form a bubble is no longer needed. This chapter investigates an air bubble with a layer of oil around it. The oil layer will contain a dye such that the particle can absorb laser light. The coating is flexible such that the whole particle can oscillate when heated by a laser beam.

In order to understand how an oil-coated bubble (stabilized by phospholipids) would behave under an oscillating laser, a simulation program was written. The main functionality of the program comes from the ideal gas law to calculate pressure, the Rayleigh-Plesset equation to find the dynamics governing the radial evolution and the heat equation to find the temperature evolution. The result is the bubble radius $Ri(t)$, temperature $T(t)$ and pressure $P(t)$ as a function of time with an input of bubble and material properties and laser power per unit area. An illustration of the simulation is given in Figure 3.1. The exact mathematics and implementation of these equations is discussed in the following.

The simulation is one dimensional which is to assume the bubble remains spherical. The initial grid consists of layers with a constant distance between them from radius (r) zero to twice the bubble size. For radii beyond this, the distance between the shells gets increasingly bigger such that the most outer grid point is so far from the bubble that one can assume the temperature and the pressure to not change. These far field properties serve as boundary conditions.

The different equations will now be derived and the forms with which they are used in the simulation will be presented.

3.1 Rayleigh-Plesset

The Rayleigh-Plesset equation describes the dynamics of a spherical bubble in a liquid. Our main objective here is to find the influence of the oil layer around the bubble and therefore a version of this equation is used that includes damping due to the oil layer. In this section the derivation of this equation presented.

3.1.1 From Navier-Stokes

The Navier-Stokes equation for an incompressible, Newtonian fluid is as follows

$$\rho\frac{Dv}{Dt} = -\nabla P + \rho g + \mu\nabla^2 v$$

Body forces will be negligible and a spherically symmetric case is investigated leading to

$$\rho\left(\frac{\partial v}{\partial t} + v\frac{\partial v}{\partial r}\right) = -\frac{\partial P}{\partial r} + \mu\nabla^2 v$$

In the simulation, the bubbles will have an oscillation amplitude in the order of micrometers and the frequency will be in the order of MHz. Speeds will therefore be approximately $1\,\mathrm{ms}^{-1}$ and thus much lower than the speed of sound. For this reason, incompressibility of the liquid is assumed and, as shown in appendix B.15,

$$v = \frac{\dot{R}R^2}{r^2}\overrightarrow{e_r}$$

Where $\dot{R}$ is $\frac{dR}{dt}$. With this we find

$$\rho\left(\frac{1}{r^2}\frac{\partial}{\partial t}(\dot{R}R^2) - 2\frac{(\dot{R}R^2)^2}{r^5}\right) = -\frac{\partial P}{\partial r} + \mu\nabla^2 v$$

$$-\frac{1}{\rho(r)}\left(\frac{\partial P}{\partial r} + \mu\nabla^2 v\right) = \frac{1}{r^2}\frac{d}{dt}\left(\dot{R}R^2\right) - \frac{2(\dot{R}R^2)^2}{r^5}$$

This equation can be written for both the oil layer and the water. When integrating from $r = A$ to $r = B$ the term $\mu\nabla^2 v$ drops out and this gives

$$\frac{P(B) - P(A)}{\rho} = \left[\frac{1}{r}\frac{d}{dt}\left(\dot{R}R^2\right) - \frac{1}{2}\frac{\left(\dot{R}R^2\right)^2}{r^4}\right]_A^B$$

$$\frac{P(B) - P(A)}{\rho} = \left[\frac{\ddot{R}R^2}{r} + \frac{2\dot{R}^2R}{r} - \frac{1}{2}\frac{\dot{R}^2R^4}{r^4}\right]_A^B$$

Taking the inner bubble radius R_i for R and the bubble radius including the oil layer R_e for A and $B = \infty$ i.e. integrating over the water part

$$P(R_e^+) - P_\infty = \rho_w \left(\frac{\ddot{R}_i R_i^2 + 2\dot{R}_i^2 R_i}{R_e} - \frac{1}{2}\frac{\dot{R}_i^2 R_i^4}{R_e^4} \right) \tag{3.1}$$

Integrating over the oil part would mean $A = R_i^+$ and $B = R_e^-$

$$\begin{aligned} P(R_e^-) - P(R_i^+) = \rho_o \Bigg(& \frac{\ddot{R}_i R_i^2 + 2\dot{R}_i^2 R_i}{R_e} - \frac{1}{2}\frac{\dot{R}_i^2 R_i^4}{R_e^4} \\ & - \left(\frac{\ddot{R}_i R_i^2 + 2\dot{R}_i^2 R_i}{R_i} - \frac{1}{2}\frac{\dot{R}_i^2 R_i^4}{R_i^4} \right) \Bigg) \end{aligned} \tag{3.2}$$

Where rewriting gives

$$\begin{aligned} P(R_i^+) - P(R_e^-) = \rho_o \Bigg(& (\ddot{R}_i R_i^2 + 2\dot{R}_i^2 Ri) \left(\frac{1}{R_i} - \frac{1}{R_e} \right) \\ & - \frac{1}{2}\dot{R}_i^2 R_i^4 \left(\frac{1}{R_i^4} - \frac{1}{R_e^4} \right) \Bigg) \end{aligned} \tag{3.3}$$

3.1.2 Normal component stress tensor

Over the oil gas interface

$$\overline{\overline{\sigma_o}} \cdot \overrightarrow{e_r} - \overline{\overline{\sigma_g}} \cdot \overrightarrow{e_r} = \delta P_1$$

Where $\overline{\overline{\sigma_o}}$ is the strain tensor and $\overrightarrow{e_r}$ denotes that it is in the r direction. δP_1 is the difference in pressure over the oil-gas interface.

$$2\mu_0 u'(R_i) - P(R_i^+) + P_g = \frac{2\sigma_o}{R_i}$$

Where u' is the velocity derivative to the radius. σ is the surface tension. Knowing $v = \dot{R}_i R_i^2/r^2$ we also know $v'(R_i) = -2\dot{R}_i R_i^2/R_i^3$

$$-4\mu_o \frac{\dot{R}_i R_i^2}{R_i^3} - P(R_i^+) + P_g = \frac{2\sigma_o}{R_i}$$

$$P_g - P(R_i^+) = 4\mu_o \frac{\dot{R}_i}{R_i} + \frac{2\sigma_o}{R_i} \tag{3.4}$$

Over the oil water interface

$$\overline{\overline{\sigma_w}} \cdot \overrightarrow{e_r} - \overline{\overline{\sigma_o}} \cdot \overrightarrow{e_r} = \delta P_2$$

$$\left[2\mu_w v'(R_e) - P(R_e^+)\right] - \left[2\mu_o v'(R_e) - P(R_e^-)\right] = \frac{2\sigma_{wo}}{R_e}$$

Knowing $v = \dot{R}_i R_i^2/r^2$ we also know $v'(R_e) = -2\dot{R}_i R_i^2/R_e^3$. Rewriting the equation above then gives

$$\left[\frac{-4\dot{R}_i R_i^2}{R_e^3}\mu_w - P(R_e^+)\right] - \left[\frac{-4\dot{R}_i R_i^2}{R_e^3}\mu_o - P(R_e^-)\right] = \frac{2\sigma_{wo}}{R_e}$$

$$\frac{-4\dot{R}_i R_i^2}{R_e^3}(\mu_w - \mu_o) - \frac{2\sigma_{wo}}{R_e} = P(R_e^+) - P(R_e^-)$$

Resulting in

$$P(R_e^+) - P(R_e^-) = \frac{4\dot{R}_i R_i^2}{R_e^3}(\mu_o - \mu_w) - \frac{2\sigma_{wo}}{R_e} \tag{3.5}$$

3.1.3 Combining for RP equation

We know that $P_g - P_\infty = P(R_i^-) - P_\infty$ because the pressure at the inside of the inner radius of the bubble is by definition in the gas and therefore $P_g \equiv P(R_i^-)$. We can rewrite by adding and subtracting similar terms

$$\begin{aligned} P_g - P_\infty = &\underbrace{P_g(R_i^-) - P(R_i^+)}_{\text{part 1}} + \underbrace{P(R_i^+) - P(R_e^-)}_{\text{part 2}} \\ &+ \underbrace{P(R_e^-) - P(R_e^+)}_{\text{part 3}} + \underbrace{P(R_e^+) - P_0}_{\text{part 4}} \end{aligned} \tag{3.6}$$

Part 1 of (3.6) is defined in (3.4), part 2 is defined in (3.3), part 3 is defined in (3.5) and part 4 is defined in (3.1). Thus, the complete equation is:

$$\begin{aligned} P_g - P_\infty = &\, 4\mu_o\frac{\dot{R}_i}{R_i} + \frac{2\sigma_o}{R_i} + \rho_o\Bigg((\ddot{R}_i R_i^2 + 2\dot{R}_i^2 Ri)\left(\frac{1}{R_i} - \frac{1}{R_e}\right) \\ &- \frac{1}{2}\dot{R}_i^2 R_i^4\left(\frac{1}{R_i^4} - \frac{1}{R_e^4}\right)\Bigg) - \frac{4\dot{R}_i R_i^2}{R_e^3}(\mu_o - \mu_w) \\ &+ \frac{2\sigma_{wo}}{R_e} + \rho_w\left(\frac{\ddot{R}_i R_i^2 + 2\dot{R}_i^2 R_i}{R_e} - \frac{1}{2}\frac{\dot{R}_i^2 R_i^4}{R_e^4}\right) \end{aligned} \tag{3.7}$$

Rewriting gives

$$\begin{aligned} P_g - P_\infty = &\, \ddot{R}_i\left[\rho_o R_i^2\left(\frac{1}{R_i} - \frac{1}{R_e}\right) + \rho_w\frac{R_i^2}{R_e}\right] \\ &+ \rho_o\left[2R_i^2 R_i\left(\frac{1}{R_i} - \frac{1}{R_e}\right) - \frac{1}{2}\dot{R}_i^2 R_i^4\left(\frac{1}{R_i^4} - \frac{1}{R_e^4}\right)\right] \\ &+ \rho_w\left[2\frac{\dot{R}_i^2 R_i}{R_e} - \frac{1}{2}\frac{\dot{R_i^2} R_i^4}{R_e^4}\right] + 4\mu_o\left[\frac{\dot{R}_i}{R_i} - \frac{\dot{R}_i R_i^2}{R_e^3}\right] + 4\frac{\dot{R}_i R_i^2}{R_e^3}\mu_w + \frac{2\sigma_{ow}}{R_e} + \frac{2\sigma_o}{R_i} \end{aligned} \tag{3.8}$$

And rewriting further

$$
\begin{aligned}
P_g - P_\infty = \ddot{R}_i &\left[\frac{R_i^2}{R_e}(\rho_w - \rho_o) + \rho_o R_i\right] \\
&+ \rho_o \left[\dot{R}_i^2 R_i \left(\frac{2}{R_i} - \frac{2}{R_e} - \frac{1}{2}\frac{1}{R_i} + \frac{1}{2}\frac{R_i^3}{R_e^4}\right)\right] + \rho_w \left[\frac{\dot{R}_i^2 R_i}{R_e}\left(2 - \frac{1}{2}\frac{R_i^3}{R_e^3}\right)\right] \\
&+ 4\mu_o \left[\frac{\dot{R}_i}{R_i} - \frac{\dot{R}_i R_i^2}{R_e^3}\right] + 4\frac{\dot{R}_i R_i^2}{R_e^3}\mu_w + \frac{2\sigma_{ow}}{R_e} + \frac{2\sigma_o}{R_i} \qquad (3.9)
\end{aligned}
$$

To reach the modified Rayleigh-Plesset equation:

$$
\begin{aligned}
P_g - P_\infty = \ddot{R}_i &\left[\frac{R_i^2}{R_e}(\rho_w - \rho_o) + \rho_o R_i\right] \\
&+ \dot{R}_i^2 R_i \left[\rho_o \left(\frac{3}{2R_i} - \frac{2}{R_e} + \frac{1}{2}\frac{R_i^3}{R_e^4}\right) + \frac{\rho_w}{R_e}\left(2 - \frac{1}{2}\frac{R_i^3}{R_e^3}\right)\right] \\
&+ 4\mu_o \left[\frac{\dot{R}_i}{R_i} - \frac{\dot{R}_i R_i^2}{R_e^3}\right] + 4\frac{\dot{R}_i R_i^2}{R_e^3}\mu_w + \frac{2\sigma_{ow}}{R_e} + \frac{2\sigma_o}{R_i} \qquad (3.10)
\end{aligned}
$$

Where the viscosity of water μ_w is temperature dependent following the following relation [14]

$$\mu_w = 2.414 \cdot 10^{-5} \cdot 10^{247.8/(T-140)}$$

Where T is the temperature of the water at the water-oil interface. This new RP equation comes down to the classic RP equation for a bubble with only one liquid around it when the properties of water and oil are chosen identical. The derivation of this is shown in appendix B.1.

3.1.4 Rayleigh-Plesset equation in the simulation

For use in the simulation, the RP equation will be rewritten to have only $\ddot{R}$ on the left side. With this equation, the new $\ddot{R}$ will be calculated with the values of $\dot{R}$ and R of the previous time iteration. The new values of $\dot{R}$ and R are then calculated as such:

$$
\begin{aligned}
\dot{R}_{t+dt} &= \dot{R}_t + \ddot{R}_t dt \\
R_{t+dt} &= R_t + \dot{R}_t dt
\end{aligned}
$$

3.1.5 The grid

The simulation works with a grid that is variable in time. The mass of each grid volume is defined to be constant and the grid is recalculated every time step to hold on to this definition. Initially, before the laser is turned on and

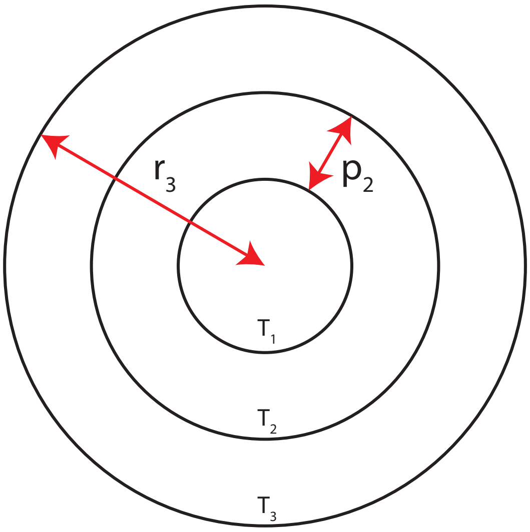

Figure 3.2: The grid defined

Figure 3.3: The grid used for the simulations. Here it can be seen that the distance between grid points is constant until twice the radius of a standard bubble (red circle). After that, the grid steps get bigger 15 % every step where in the real simulation the biggest grid radius is more than 3000 times the standard bubble size and there are 96 grid-circles within the standard bubble size.

before the bubble starts to oscillate, the grid is defined with a regular size interval of 31.25 nm up to a radius of 6 µm which is twice the typical bubble radius. Beyond this radius the grid gets 15 % bigger each step outward. This way, without having an excessive amount of grid points, the most outer grid point is more than 3000 times the typical bubble radius.

3.2 The ideal gas law

3.2.1 Constant in time

In order to find an expression for the pressure, we look at the ideal gas law:

$$PV = \frac{m}{\tilde{\mu}} R_g T$$

where P is pressure, V is volume, m is mass, $\tilde{\mu}$ is the molar mass in kilograms per mole, R_g is the ideal gas constant. The simulation is defined such that the mass in each grid-volume remains constant in time. As mentioned before, the speed of the bubble wall $\dot{R}$ is much smaller than the speed of sound. Therefore the pressure in the bubble is considered homogeneous. With this information it can be shown that the pressure is defined as such.

$$P = \frac{P_0}{T_0} \frac{4}{3} \pi R_0^3 \frac{1}{\sum V_k / T_k}$$

where $\sum V_k/T_k$ can be defined as

$$\sum \frac{V_k}{T_k} = \sum \frac{4}{3} \pi \frac{(r_{k-1} + p_k)^3 - r_{k-1}^3}{T_k},$$

where subscript 0 stands for the initial value before the laser is turned on. In appendix B.2 all the intermediate mathematical steps are shown.

3.2.2 Constant in radius

Gas regime

As mentioned before, the pressure is constant with respect to the radius inside the bubble. This tells us

$$\frac{V_k}{m_k T_k} = \text{constant}(r)$$

Further rewriting and using that m_k is constant in time, gives

$$r_{k-1} = \left(-\frac{R_g}{\tilde{\mu} P} \rho_0 T_k \left[(k p_0)^3 - ((k-1)\, p_0)^3 \right] + r_k^3 \right)^{1/3}$$

Where r_k is the radius in meters that belongs to grid point k. To speed up the calculation in Matlab or Fortran, an approximation based on a Taylor expansion is made from which we find

$$r_{k-1} = r_k \left(1 + \frac{1}{3} H - \frac{1}{9} H^2 + \frac{10}{162} H^3 \right)$$

with

$$H = -\frac{R_g}{\tilde{\mu} P} \rho_0 T_k \frac{1}{{r_k}^3} \left[(k p_0)^3 - ((k-1)\, p_0)^3 \right] \tag{3.11}$$

All detailed mathematical steps can be found in appendix B.3.

Outer regime

The mass in each grid volume is defined to be constant over time, the oil and the water is assumed incompressible and therefore the volume in each grid volume in the oil and water regime is constant in time. With this information the grid can be redefined at each time step:

$$r_{k+1} = \left(\left[\left((k+1)\, p_0 \right)^3 - \left(k p_0 \right)^3 \right] + r_k^3 \right)^{1/3}$$

And in a similar fashion as what has been done before, this can be Taylor expanded to give

$$r_{k+1} = r_k \left(1 + \frac{1}{3} H - \frac{1}{9} H^2 + \frac{10}{162} H^3 \right),$$

with

$$H = \left[\left((k+1)\, p_0 \right)^3 - \left(k p_0 \right)^3 \right] \frac{1}{r_k}^3 . \tag{3.12}$$

3.3 The heat equation

The basic heat equation

$$D \nabla^2 T + \frac{I}{\rho c_p} = \frac{DT}{Dt},$$

where I is in units of Wm^{-3}. Since the simulation calculates the temperature for each grid point, and the grid points move along with the movement of mass, the total derivative becomes an ordinary partial derivative. Furthermore, the simulation is only in the r direction making the heat equation:

$$D \frac{1}{r^2} \frac{\partial}{\partial r} \left(r^2 \frac{\partial T}{\partial r} \right) + \frac{I}{\rho c_p} = \frac{\partial T}{\partial t}. \tag{3.13}$$

This can be approximated with a central difference scheme in space and a forward finite difference scheme in time resulting in

$$T_k^{n+1} = \frac{dtD}{r_k^2} \left[\frac{ \left((r_k + \frac{1}{2} p_{k+1})^2 \frac{T_{k+1} - T_k}{p_{k+1}} \right) - \left((r_{k-1} + \frac{1}{2} p_k)^2 \frac{T_k - T_{k-1}}{p_k} \right) }{ \frac{1}{2} p_k + \frac{1}{2} p_{k+1} } \right] + \frac{dtI}{\rho c_p} + T_k^n \tag{3.14}$$

The full mathematical derivation of this can be found in appendix B.4. In the simulation it can now be used that the new temperature at grid point k

in terms of the old temperature in the grid points $k-1$, k, $k+1$ is as follows:

$$T_k^{n+1} = T_{k-1}^n \left[\frac{dtD}{r_k^2} \frac{\left(r_{k-1} + \frac{1}{2}p_k)\right)^2}{p_k\left(\frac{1}{2}p_k + \frac{1}{2}p_{k+1}\right)} \right]$$

$$+ T_k^n \left[1 - \frac{dtD}{r_k^2\left(\frac{1}{2}p_k + \frac{1}{2}p_{k+1}\right)} \left(\frac{\left(r_k + \frac{1}{2}p_{k+1})\right)^2}{p_{k+1}} + \frac{\left(r_{k-1} + \frac{1}{2}p_k)\right)^2}{p_k} \right) \right]$$

$$+ T_{k+1}^n \left[\frac{dtD}{r_k^2\left(\frac{1}{2}p_k + \frac{1}{2}p_{k+1}\right)} \frac{\left(r_k + \frac{1}{2}p_{k+1})\right)^2}{p_{k+1}} \right]$$

$$+ \frac{dtI}{\rho c_p}. \quad (3.15)$$

3.3.1 Second order precision over the gas-oil interface and the oil-water interface.

The heat equation that was defined above can be used as long as the temperature is known at grid points $k+1$, k and $k-1$. This works except right next to an interface where one of these values is missing. When crossing the interface between gas and oil, or between oil and water the heat equation must be defined separately. These equations will be based on a second order Taylor expansion and are therefore more precise than the heat equation for the bulk. This is required for the program to be stable.

Outer side of an interface

First we look at the outer side of an interface for which grid point values greater or equal to k are known. Just like in the heat equation for the bulk, we express the new temperature T_k^{n+1} in terms of the old temperature on three grid points T_k^n,$T_{k\ 1}^n$ and T_{k+2}^n.

$$T_k = T_k \quad \text{(a)}$$

Using a Taylor expansion up to second order to get enough precision

$$T_{k+1} = T_k + p_{k+1}T_k' + \frac{p_{k+1}^2}{2}T_k'' \quad \text{(b)}$$

$$T_{k+2} = T_k + \left(p_{k+1} + p_{k+2}\right)T_k' + \frac{\left(p_{k+1} + p_{k+2}\right)^2}{2}T_k'' \quad \text{(c)}$$

The heat flux across the oil water interface must be conserved leading to the following condition:

$$\lambda_o \frac{\partial T_o}{\partial r}|_{R_e} = \lambda_w \frac{\partial T_w}{\partial r}|_{R_e}$$

We therefore need to know the derivative of the temperature with respect to the radius. To find this we look for $T'_k = A \cdot a + B \cdot b + C \cdot c$ with the capital letters being coefficients and the small letters being the equations presented above, i.e. $T'_k = A \cdot T_k + B \cdot T_{k+1} + C \cdot T_{k+2}$. A, B and C should therefore be such that T_k is zero, T'_k is one and T''_k is zero. This results in

$$\begin{aligned}
A &= -\frac{(p_{k+1} + p_{k+2})}{p_{k+1}p_{k+2}} - \frac{1}{(p_{k+1} + p_{k+2}) - \dfrac{(p_{k+1} + p_{k+2})^2}{p_{k+1}}}, \\
B &= \frac{(p_{k+1} + p_{k+2})}{p_{k+1}p_{k+2}}, \\
C &= \frac{1}{(p_{k+1} + p_{k+2}) - \dfrac{(p_{k+1} + p_{k+2})^2}{p_{k+1}}}.
\end{aligned}$$

More mathematical steps are shown in appendix B.5.

Inner side of an interface

Until now we considered the temperature to be known for grid points k or higher. This is the case when looking at the outer side of a boundary. For looking at the inner side of a boundary grid points bigger than k are not known and the same analysis can be done for this side as is shown in appendix B.6. The results are an expression like $T'_k = A \cdot T_k + B \cdot T_{k-1} + C \cdot T_{k-2}$ Where D, E and F are

$$\begin{aligned}
D &= \frac{(p_k + p_{k-1})}{p_k p_{k-1}} - \frac{1}{\dfrac{(p_k + p_{k-1})^2}{p_k} - (p_k + p_{k-1})}, \\
E &= -\frac{(p_k + p_{k-1})}{p_k p_{k-1}}, \\
F &= \frac{1}{\dfrac{(p_k + p_{k-1})^2}{p_k} - (p_k + p_{k-1})}.
\end{aligned}$$

Resulting interface conditions in the simulation

The boundary condition between the oil and the water is the following

$$\lambda_o \frac{\partial T_o}{\partial r}|_{R_e} = \lambda_w \frac{\partial T_w}{\partial r}|_{R_e},$$

with R_e being the radius of the bubble at the oil water interface. Filling in for what was found in the previous section

$$\lambda_o \left(DT_k + ET_{k-1} + FT_{k-2}\right) = \lambda_w \left(AT_k + BT_{k+1} + CT_{k+2}\right)$$

Rearranging gives:

$$T_k = \frac{-\lambda_o \left(ET_{k-1} + FT_{k-2}\right) + \lambda_w \left(BT_{k+1} + CT_{k+2}\right)}{\lambda_o D - \lambda_w A},$$

with k being the gridpoint on the boundary between water and oil. Similarly, the boundary condition between the oil and the gas is

$$\lambda_g \frac{\partial T_g}{\partial r}|_{R_i} = \lambda_o \frac{\partial T_o}{\partial r}|_{R_i}$$

with R_i being the radius of the bubble at the gas–oil interface. Rearranging this gives

$$T_k = \frac{-\lambda_g \left(ET_{k-1} + FT_{k-2}\right) + \lambda_o \left(BT_{k+1} + CT_{k+2}\right)}{\lambda_g D - \lambda_o A}.$$

3.4 Static bubble solution

This part is done to examine what the equilibrium temperature is of the bubble with the laser continuously on. When the simulation converges (in the limit) to this temperature it can be concluded the program is correct. This is of course assuming this simplified calculation is correct. It starts with the heat equation, taken from (3.13).

$$D \frac{1}{r^2} \frac{\partial}{\partial r} \left(r^2 \frac{\partial T}{\partial r} \right) + \frac{I}{\rho c_p} = \frac{DT}{Dt}$$

Normally I (Wm^{-3}) would be a function of time but in this static solution it is taken to be the average laser power. In case the laser is modulated as a sine wave I would be half the maximum laser power. Because we are interested in the stationary equilibrium case the temperature change in time is zero:

$$D \left(\frac{2}{r} \frac{\partial T}{\partial r} + \frac{\partial^2 T}{\partial r^2} \right) + \frac{I}{\rho c_p} = 0$$

An expression for T can be given as a solution to this differential equation

$$T = \frac{-Ir^2}{6 c_p D \rho} - \frac{C_1}{r} + C_2,$$

where C_1 and C_2 are constants. From this the equilibrium temperature profile can be found when taking into account that the temperature in the gas is homogeneous and because of that the derivative with respect to the radius of the temperature in oil at the gas side is zero. Furthermore, the temperature of the water at $r = \infty$ does not change, the temperature at two sides of the interface is the same and the boundary condition between oil and water is the following:

$$\lambda_o \frac{\partial T_o}{\partial r}|_{R_e} = \lambda_w \frac{\partial T_w}{\partial r}|_{R_e}$$

The found equilibrium temperature profile:

$$T_{gas,eq} = \frac{-IR_{i,eq}^2}{6\lambda_o} - \frac{C_{1o}}{R_{i,eq}} + C_{2o}, \tag{3.16}$$

$$T_{water,eq} = \frac{1}{r}\left(\frac{-IR_{e,eq}^3}{6\lambda_o} - C_{1o} + R_{e,eq}C_{2o}\right), \tag{3.17}$$

$$T_{oil,eq} = \frac{-Ir^2}{6\lambda_o} - \frac{C_{1o}}{r} + C_{2o}, \tag{3.18}$$

with

$$C_{1o} = \frac{IR_{i,eq}^3}{3\lambda_o},$$

$$C_{2o} = \frac{C_{1o}}{R_{e,eq}}\left(1 - \frac{\lambda_o}{\lambda_w}\right) + \frac{IR_{e,eq}^2}{3\lambda_o}\left(0.5 + \frac{\lambda_o}{\lambda_w}\right).$$

Subscript *eq* was added to indicate this is the equilibrium value. All mathematical steps are shown in appendix B.11.

An example simulation is shown in Figure 3.4. The static solution is chosen to have an equilibrium value of 3.1 µm and the simulation converges nicely to the found temperature profile.

An equation for the equilibrium radius can be found by taking into account the state equation and the expression for the pressure being the atmospheric pressure plus the two Laplace pressures. As shown in appendix B.13, the expression for the equilibrium radius is

$$R_{i,eq} = R_{i,0}\left[\frac{T_{gas,eq}P_0}{T_0\left(P_\infty + \frac{2\sigma_{go}}{R_{i,eq}} + \frac{2\sigma_{ow}}{R_{e,eq}}\right)}\right]^{1/3}$$

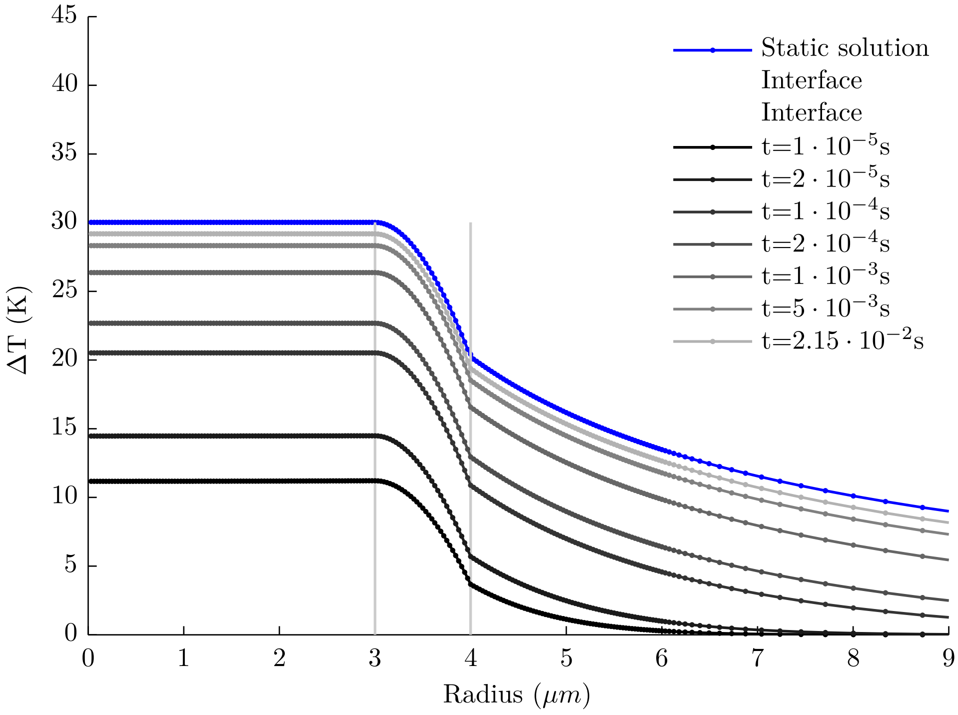

Figure 3.4: The simulated result converges to the static solution. This simulation is done for a 3 µm bubble with a 1 µm thick triacetin oil layer and shining the laser continuously

3.4.1 Finding equilibrium temperature as a function of laser power

We would like to know the equilibrium gas temperature as a function of laser power. From (3.16) we have an expression for the equilibrium gas temperature as a function of R_i and laser power. From (B.19) we have another expression for the equilibrium gas temperature as a function of R_i but not of laser power. These can be equated as shown in appendix B.7 leading to an expression that is more easily solved numerically than analytically. Therefore, a matlab script was written to find the equilibrium gas temperature as a function of laser power. When this is done for a bubble with initial inner radius of 3 µm, a triacetin oil layer 1 µm thick and the laser continuously radiating at $10^{10}\,\mathrm{Wm^{-2}}$, an equilibrium radius is found to be 3.0977 µm. In Figure 3.4 it can be seen that the simulation does converge to this value and the predicted temperature profile.

3.5 Small variations around equilibrium: The simplified model

In this part small variations are added to the static solution in order to obtain a simple model describing the simulation result. The full simulation calculates everything from room temperature but this simplified model only calculates what the equilibrium values should be from the static solution. From there the oscillations are calculated.

The static solution assumes the temperature in the gas to be homogeneous. For this to also be true for a modulated laser signal, the diffusion time of the heat in the gas should be smaller than the half period of the laser modulation. This can be contained in the following equations

$$t = \frac{R_i^2}{2\pi D_g} = \frac{\text{Period laser}}{2} = \frac{1}{2f},$$

$$R_{i,limit} = \sqrt{\frac{\pi D_g}{f}},$$

leading to a maximum bubble radius for which the static solution including laser modulation is still valid for a distance just over 6 µm. The same calculation can be done for the water to find a diffusion distance of 0.1 µm.

The change in temperature over time can be described as follows:

$$(\rho_o V_{oil} C_{po} + \rho_w V_{w0.1} C_{pw})\, dT = (B - B_0/2) \cdot V_{oil} dt,$$

with ρ_o the density of the oil, $V_{w0.1}$ the volume of the first 0.1 µm of water, C_{po} the heat capacity at constant pressure of the oil, B_0 the maximum power of the laser and B the absorbed laser power ($\mathrm{Wm^{-3}}$). In the simulation the laser is modulated as a step function. But, because all functions can be described by a combination of sine waves, a sinusoidal modulation is chosen in this case. This means B becomes a sine function.

$$\frac{dT}{dt}=\frac{(B-B_0/2)\cdot V_{oil}}{\rho_o V_{oil}C_{po}+\rho_w V_{w0.1}C_{pw}}=\frac{B_{amp}\cos(\omega t)\cdot V_{oil}}{\rho_o V_{oil}C_{po}+\rho_w V_{w0.1}C_{pw}} \tag{3.19}$$

As described in appendix B.14, from this, an equation describing the behavior of the bubbles can be found by using equations B.19 (the gas in each grid volume remaining constant) and 3.10 (the modified Rayleigh-Plesset equation).

$$\begin{aligned}
&\frac{P_0V_0}{T_0\frac{4}{3}\pi R_i^3}\Bigg[\frac{B_{amp}\sin(\omega t)\cdot V_{oil}}{\omega\left(\rho_o V_{oil}C_{po}+\rho_w V_{w0.1}C_{pw}\right)}\\
&+\frac{B_{amp}}{3\lambda_o}\left(-1.5R_{i,eq}^2+\frac{R_{i,eq}^3}{R_{e,eq}}\left(1-\frac{\lambda_o}{\lambda_w}\right)+R_{e,eq}^2\left(0.5+\frac{\lambda_o}{\lambda_w}\right)\right)+T_{room}\Bigg]\\
&-P_\infty=\ddot{R}_i\left[\frac{R_i^2}{R_e}(\rho_w-\rho_o)+\rho_oR_i\right]+\dot{R}_i^2R_i\Bigg[\rho_o\left(\frac{3}{2R_i}-\frac{2}{R_e}+\frac{1}{2}\frac{R_i^3}{R_e^4}\right)\\
&+\frac{\rho_w}{R_e}\left(2-\frac{1}{2}\frac{R_i^3}{R_e^3}\right)\Bigg]+4\mu_o\left[\frac{\dot{R}_i}{R_i}-\frac{\dot{R}_iR_i^2}{R_e^3}\right]+4\frac{\dot{R}_iR_i^2}{R_e^3}\mu_w+\frac{2\sigma_{ow}}{R_e}+\frac{2\sigma_o}{R_i}
\end{aligned} \tag{3.20}$$

3.6 Linear solution

From (3.19) we know

$$\frac{dT}{dt}=\frac{(B-B_0/2)\cdot V_{oil}}{\rho_o V_{oil}C_{po}+\rho_w V_{w0.1}C_{pw}} \tag{3.21}$$

$$\rightarrow T_g=\frac{\int Bdt}{\rho_oC_{po}+\rho_w\frac{V_{w0.1}}{V_{oil}}C_{pw}}+T_{gas,eq}+T_{room} \tag{3.22}$$

We also know from (B.24)

$$P_g=\frac{P_0V_0T_g}{T_0\frac{4}{3}\pi R_i^3} \tag{3.23}$$

And from (B.25)

$$\begin{aligned}
P_g-P_\infty&=\ddot{R}_i\left[\frac{R_i^2}{R_e}(\rho_w-\rho_o)+\rho_oR_i\right]+\dot{R}_i^2R_i\Bigg[\rho_o\left(\frac{3}{2R_i}-\frac{2}{R_e}+\frac{1}{2}\frac{R_i^3}{R_e^4}\right)\\
&+\frac{\rho_w}{R_e}\left(2-\frac{1}{2}\frac{R_i^3}{R_e^3}\right)\Bigg]+4\mu_o\left[\frac{\dot{R}_i}{R_i}-\frac{\dot{R}_iR_i^2}{R_e^3}\right]+4\frac{\dot{R}_iR_i^2}{R_e^3}\mu_w+\frac{2\sigma_{ow}}{R_e}+\frac{2\sigma_o}{R_i}
\end{aligned} \tag{3.24}$$

giving

$$\frac{P_0V_0}{T_0\frac{4}{3}\pi R_i^3}\left[\frac{\int Bdt}{\rho_oC_{po}+\rho_w\frac{V_{w0.1}}{V_{oil}}C_{pw}}+T_{gas,eq}+T_{room}\right]-P_\infty$$
$$=\ddot{R}_i\left[\frac{R_i^2}{R_e}(\rho_w-\rho_o)+\rho_oR_i\right]+\dot{R}_i^2R_i\left[\rho_o\left(\frac{3}{2R_i}-\frac{2}{R_e}+\frac{1}{2}\frac{R_i^3}{R_e^4}\right)+\frac{\rho_w}{R_e}\left(2-\frac{1}{2}\frac{R_i^3}{R_e^3}\right)\right]$$
$$+4\mu_o\left[\frac{\dot{R}_i}{R_i}-\frac{\dot{R}_iR_i^2}{R_e^3}\right]+4\frac{\dot{R}_iR_i^2}{R_e^3}\mu_w+\frac{2\sigma_{ow}}{R_e}+\frac{2\sigma_o}{R_i} \tag{3.25}$$

Organizing for $\dot{R}$, $\dot{R}^2$ and $\ddot{R}$ and, as an approximation, taking all R_i and R_e to be $R_{i,eq}$ and $R_{e,eq}$ in case they are multiplied by $\dot{R}$, $\dot{R}^2$ or $\ddot{R}$.

$$\int Bdt\ \underbrace{\left[\frac{P_0V_0}{T_0\frac{4}{3}\pi R_{i,eq}^3\left(\rho_oC_{po}+\rho_w\frac{V_{w0.1}}{V_{oil}}C_{pw}\right)}\right]}_{\alpha}+\frac{P_0V_0}{T_0\frac{4}{3}\pi R_i^3}\left[T_{gas,eq}+T_{room}\right]-P_\infty$$
$$=\ddot{R}_i\underbrace{\left[\frac{R_{i,eq}^2}{R_{e,eq}}(\rho_w-\rho_o)+\rho_oR_{i,eq}\right]}_{\beta}$$
$$+\dot{R}_i^2\underbrace{R_{i,eq}\left[\rho_o\left(\frac{3}{2R_{i,eq}}-\frac{2}{R_{e,eq}}+\frac{1}{2}\frac{R_{i,eq}^3}{R_{e,eq}^4}\right)+\frac{\rho_w}{R_{e,eq}}\left(2-\frac{1}{2}\frac{R_{i,eq}^3}{R_{e,eq}^3}\right)\right]}_{\gamma}$$
$$\dot{R}_i\underbrace{\left[4\left(\frac{\mu_o}{R_{i,eq}}+\frac{R_{i,eq}^2}{R_{e,eq}^3}\left(\mu_w-\mu_o\right)\right)\right]}_{\delta}$$
$$+2\frac{\sigma_{ow}}{R_e}+\frac{\sigma_o}{R_i} \tag{3.26}$$

In order to find an equation that does not contain an integral, everything is derived to time.

$$\alpha B-\underbrace{3\frac{P_0T_{g2}}{T_0}\frac{R_{i,0}}{R_{i,eq}^4}}_{\zeta}\dot{R}_i\ =\ \dddot{R}_i\beta\ +\ 2\gamma\ddot{R}_i\dot{R}_i\ +\ \delta\ddot{R}_i\ +\ 2\dot{R}_i\underbrace{\left(\frac{-\sigma_{ow}}{R_e^2}+\frac{-\sigma_o}{R_i^2}\right)}_{\epsilon} \tag{3.27}$$

$$\alpha B-\zeta\dot{R}_i=\dddot{R}_i\beta+2\gamma\ddot{R}_i\dot{R}_i+\delta\ddot{R}_i+2\dot{R}_i\epsilon \tag{3.28}$$

In which case $\dot{R}_e$ is assumed to be approximately $\dot{R}_i$ and $T_{gas,eq}+T_{room}$ is now called T_{g2}. The term $2\gamma\ddot{R}_i\dot{R}_i$ is of higher order and is therefore neglected.

R_i is expected to act as an harmonic oscillator and will therefore have the shape of

$$R_i = R_{i,eq} + r_i e^{j\omega t} + \varphi = R_{i,eq} + \underline{ri} \tag{3.29}$$

$$\dot{R}_i = j\omega r_i e^{j\omega t} + \varphi = (j\omega)\underline{ri} \tag{3.30}$$

$$\ddot{R}_i = -\omega^2 r_i e^{j\omega t} + \varphi = (j\omega)^2\underline{ri} \tag{3.31}$$

$$\dddot{R}_i = -j\omega^3 r_i e^{j\omega t} + \varphi = (j\omega)^3\underline{ri} \tag{3.32}$$

$$\alpha B = j\omega r_i \left[2\epsilon + \zeta + jw\delta - \omega^2\beta\right] \tag{3.33}$$

$$\frac{r_i}{B} = \frac{\alpha/(2\epsilon + \zeta)}{j\omega\left[1 + jw\dfrac{\delta}{2\epsilon + \zeta} - \omega^2\dfrac{\beta}{2\epsilon + \zeta}\right]} \tag{3.34}$$

Which has the shape of a transfer function

$$\frac{O}{I} = \frac{G}{1 + j\omega\dfrac{2z}{\omega_0} - \dfrac{\omega^2}{\omega_o^2}} \cdot \frac{1}{j\omega} \tag{3.35}$$

with G being the gain, O the output, I the input, z the damping and ω_0 the angular eigen frequency. One thing that can be noted here is that this transfer function is of third order where a standard RP equation would be of second order. The expected phase difference in our case is therefore π at resonance instead of $\pi/2$ such as in the normal RP equation.

$$\rightarrow \omega_0 = \sqrt{\frac{2\epsilon + \zeta}{\beta}} = \sqrt{\frac{-2\left(\dfrac{\sigma_{ow}}{R_e^2} + \dfrac{\sigma_o}{R_i^2}\right) + 3\dfrac{P_0 T_{g2}}{T_0}\dfrac{R_{i,0}}{R_{i,eq}^4}}{\dfrac{R_{i,eq}^2}{R_{e,eq}}(\rho_w - \rho_o) + \rho_o R_{i,eq}}} \tag{3.36}$$

From (B.24) we can find

$$\frac{T_{g2} R_{i,0}^3}{R_{i,eq}^4} = \frac{T_0 P_{g,eq}}{P_0 R_{i,eq}} \tag{3.37}$$

Therefore ζ can be simplified

$$\zeta = 3\frac{P_0}{T_0}\frac{T_{g2} R_{i,0}}{R_{i,eq}^4} = 3\frac{P_{g,eq}}{R_{i,eq}} \tag{3.38}$$

Where the equilibrium pressure $P_{g,eq}$ is the atmospheric pressure plus the two Laplace pressures. This can be filled in giving

$$\zeta = 3\left(\frac{P_{atm}}{R_{i,eq}} + \frac{2\sigma_o}{R_{i,eq}^2} + \frac{2\sigma_{ow}}{R_{i,eq} R_{e,eq}}\right) \tag{3.39}$$

$$\rightarrow \omega_0 = \sqrt{\frac{-2\left(\frac{\sigma_{ow}}{R_{e,eq}^2}+\frac{\sigma_o}{R_{i,eq}^2}\right)+3\left(\frac{P_{atm}}{R_{i,eq}}+\frac{2\sigma_o}{R_{i,eq}^2}+\frac{2\sigma_{ow}}{R_{i,eq}R_{e,eq}}\right)}{\frac{R_{i,eq}^2}{R_{e,eq}}(\rho_w-\rho_o)+\rho_o R_{i,eq}}} \tag{3.40}$$

ω_0 is not a function of time so all R_i and R_e are now $R_{i,eq}$ and $R_{e,eq}$.

$$\rightarrow \omega_0 = \sqrt{\frac{\frac{4\sigma_o}{R_{i,eq}^2}+2\sigma_{ow}\left(\frac{-1}{R_{e,eq}^2}+\frac{3}{R_{i,eq}R_{e,eq}}\right)+\frac{3P_{atm}}{R_{i,eq}}}{\frac{R_{i,eq}^2}{R_{e,eq}}(\rho_w-\rho_o)+\rho_o R_{i,eq}}} \tag{3.41}$$

$$\rightarrow \omega_0 = \sqrt{\frac{\frac{1}{R_{i,eq}}\left(\frac{4\sigma_o}{R_{i,eq}}+2\sigma_{ow}\left(\frac{-R_{i,eq}}{R_{e,eq}^2}+\frac{3}{R_{e,eq}}\right)+3P_{atm}\right)}{R_{i,eq}\left(\frac{R_{i,eq}}{R_{e,eq}}(\rho_w-\rho_o)+\rho_o\right)}} \tag{3.42}$$

$$\rightarrow \omega_0 = \frac{1}{R_{i,eq}}\sqrt{\frac{\frac{4\sigma_o}{R_{i,eq}}+2\sigma_{ow}\left(\frac{-R_{i,eq}}{R_{e,eq}^2}+\frac{3}{R_{e,eq}}\right)+3P_{atm}}{\frac{R_{i,eq}}{R_{e,eq}}(\rho_w-\rho_o)+\rho_o}} \tag{3.43}$$

which altogether is an expression for the angular eigenfrequency as a function of $R_{i,eq}$ and $R_{e,eq}$. This shows the eigenfrequency is inversely related to the bubble size but also shows that the oil layer thickness plays a role. The denominator under the square root shows an inertial shift of the resonance curve: Because oil and water have different densities, the thickness of the oil layer influences the mass to be displaced and therefore the resonance frequency.

Now to find an expression for the damping. According to 3.35:

$$\frac{2z}{\omega_0} = \frac{\delta}{2\epsilon+\zeta} \tag{3.44}$$

$$\omega_0 = \sqrt{\frac{2\epsilon+\zeta}{\beta}} \tag{3.45}$$

$$\rightarrow z = \frac{\omega_0}{2}\frac{\delta}{2\epsilon+\zeta} = \frac{1}{2}\frac{\delta}{\sqrt{\beta(2\epsilon+\zeta)}} \tag{3.46}$$

$$z = \frac{1}{2}\frac{4\left(\frac{\mu_o}{R_{i,eq}}+\frac{R_{i,eq}^2}{R_{e,eq}^3}(\mu_w-\mu_o)\right)}{\sqrt{\beta(2\epsilon+\zeta)}} \tag{3.47}$$

The next part will be about founding out if there is an optimum response. This starts by looking at the gain of the transfer function which was found to be $\alpha/(2\epsilon + \zeta)$. From (3.26) we know

$$\alpha = \left[\frac{P_0 R_{i,0}^3}{T_0 R_{i,eq}^3 \left(\rho_o C_{po} + \rho_w \dfrac{V_{w0.1}}{V_{oil}} C_{pw}\right)}\right] \tag{3.48}$$

The factor $V_{w0.1}/V_{oil}$ never changes much and there is no maximum in $R_{i,eq}$ because there is no maximum in T_{g2}. The gain therefore has no maximum We now assume damping is small and, because $\omega_r = \omega_0\sqrt{1 - 2z^2}$, the resonance frequency is therefore approximately the eigenfrequency. The transfer function then becomes

$$\frac{r_i}{B} = \frac{\alpha/(2\epsilon + \zeta)}{j\omega \left[1 + jw \dfrac{\delta}{2\epsilon + \zeta} - 1\right]} \tag{3.49}$$

$$\frac{r_i}{B} = \frac{\alpha/(2\epsilon + \zeta)}{-2\omega_0 z} \tag{3.50}$$

$$2\omega_0 z = 2\sqrt{\frac{2\epsilon + \zeta}{\beta}} \cdot \frac{1}{2} \frac{\delta}{\sqrt{\beta(2\epsilon + \zeta)}} = \sqrt{\frac{1}{\beta}} \cdot \frac{2}{2} \frac{\delta}{\sqrt{\beta}} = \frac{\delta}{\beta} \tag{3.51}$$

$$= \frac{4\left(\dfrac{\mu_o}{R_{i,eq}} + \dfrac{R_{i,eq}^2}{R_{e,eq}^3}(\mu_w - \mu_o)\right)}{\dfrac{R_{i,eq}^2}{R_{e,eq}}(\rho_w - \rho_o) + \rho_o R_{i,eq}} \tag{3.52}$$

$$= \frac{4/R_{i,eq}\left(\mu_o + \dfrac{R_{i,eq}^3}{R_{e,eq}^3}(\mu_w - \mu_o)\right)}{R_{i,eq}\left(\dfrac{R_{i,eq}}{R_{e,eq}}(\rho_w - \rho_o) + \rho_o\right)} \tag{3.53}$$

$$= \underbrace{\frac{4}{R_{i,eq}^2}}_{(2)} \underbrace{\frac{\mu_o + \dfrac{R_{i,eq}^3}{R_{e,eq}^3}(\mu_w - \mu_o)}{\dfrac{R_{i,eq}}{R_{e,eq}}(\rho_w - \rho_o) + \rho_o}}_{(3)} \tag{3.54}$$

In this equation part (2) is not a function of the thickness of the oil and part (3) is a function of the thickness of the oil in case $R_{i,eq}$ is fixed. In order to find if there is an optimum oil layer thickness we only look at part (3).

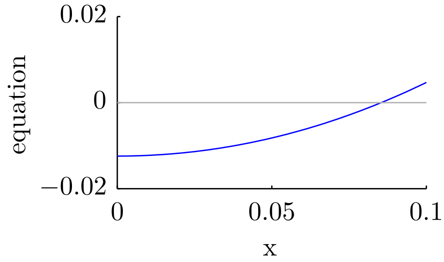

Figure 3.5: $\dfrac{d(3)}{dt}$ for heptane

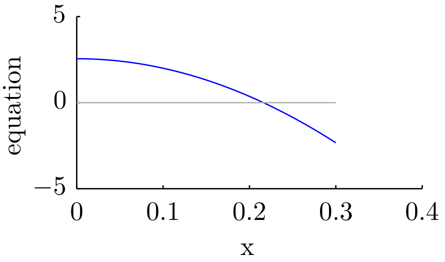

Figure 3.6: $\dfrac{d(3)}{dt}$ for triacetin

Introducing the variable $x = \dfrac{R_{i,eq}}{R_{e,eq}}$

$$(3) = \frac{\mu_o + (\mu_w - \mu_o)\, x^3}{\rho_o + (\rho_w - \rho_o)x} \tag{3.55}$$

To find the extremum:

$$\frac{d(3)}{dx} = 0 = \frac{3x^2(\mu_w - \mu_o)(\rho_o + (\rho_w - \rho_o)x) - (\mu_o + (\mu_w - \mu_o)x^3)(\rho_w - \rho_o)}{(\rho_o + (\rho_w - \rho_o)x)^2} \tag{3.56}$$

$$\rightarrow x^2\,(3(\mu_w - \mu_o)\rho_o) + x^3(3(\mu_w - \mu_o)(\rho_w - \rho_o) - (\mu_w - \mu_o)(\rho_w - \rho_o)) - \mu_o(\rho_w - \rho_o) = 0 \tag{3.57}$$

$$\rightarrow x^3\,\underbrace{(2(\mu_w - \mu_o)(\rho_w - \rho_o))}_{(a)} + x^2\,\underbrace{(3(\mu_w - \mu_o)\rho_o)}_{(b)} - \underbrace{\mu_o(\rho_w - \rho_o)}_{(c)} = 0 \tag{3.58}$$

We are looking for an optimum in x so part (c) is not important. In case of heptane oil at 300 K, part (a) has a value of approximately 0.5 and part (b) is approximately 1.7. In case of triacetin, $(a) \approx 5$ and $(b) \approx -56$. The result of this can be seen in Figures 3.5 and 3.6 and from this is can be concluded that for heptane oil there is a minimum radial amplitude for a given value of $R_{i,eq}/R_{e,eq}$ but no maximum. For triacetin there is a maximum but no minimum. Because part (3) is part of the denominator of the transfer function, a minimum would be an optimum response. In other words: it is expected that there is an optimum oil layer thickness in case of heptane but there is no expected optimum for triacetin oil.

3.7 Simulation results

A typical simulation result is shown in Figures 3.7, 3.8 and 3.10. This result is for a 3 µm radius bubble and as will be shown later, is very close to the resonance peak. The bubble is coated with a 1 µm thick heptane oil layer is immersed in a water bath of room temperature (300 K). A 10^{10} Wm^{-2} laser

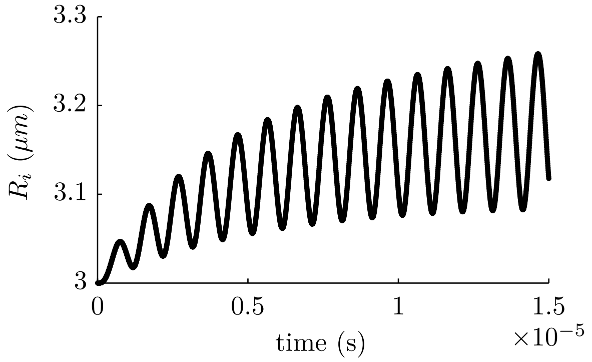

Figure 3.7: Simulation result of a bubble under standard conditions with heptane oil.

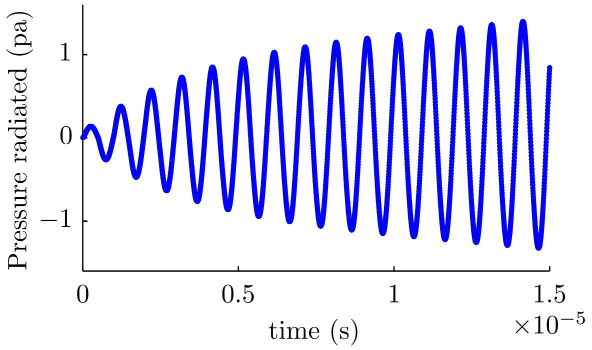

Figure 3.8: Simulation result of a bubble under standard conditions with heptane oil.

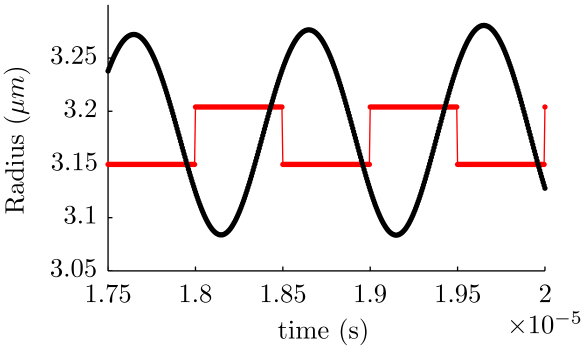

Figure 3.9: A demonstration of the phase difference between the radial response of the bubble and the laser. The black line shows the radius as a function of time just like in Figure 3.7. The red line shows the power of the laser where high is on and a low line means the laser is off.

is turned on and off with a frequency of 1 MHz. The oil layer contains just enough dye to prevent boiling at all times: with an absorption coefficient (μ) of 2700 m^{-1} the temperature remains smaller than 373 K. These conditions will later be referred to as ‘standard conditions’ and a complete overview of all standard parameters is given in appendix A. In practice, more dye can be dissolved in this oil layer such that the absorption coefficient would go up to 6000 m^{-1} but this value is chosen to keep the temperature below boiling because the simulation does not take vaporization into account and the results are therefore not valid above boiling temperatures.

In Figure 3.9 the radius-time curve for a typical bubble is shown again, this time together with the laser modulation. It can be seen that the phase difference between laser modulation and bubble radius is close to π. This was

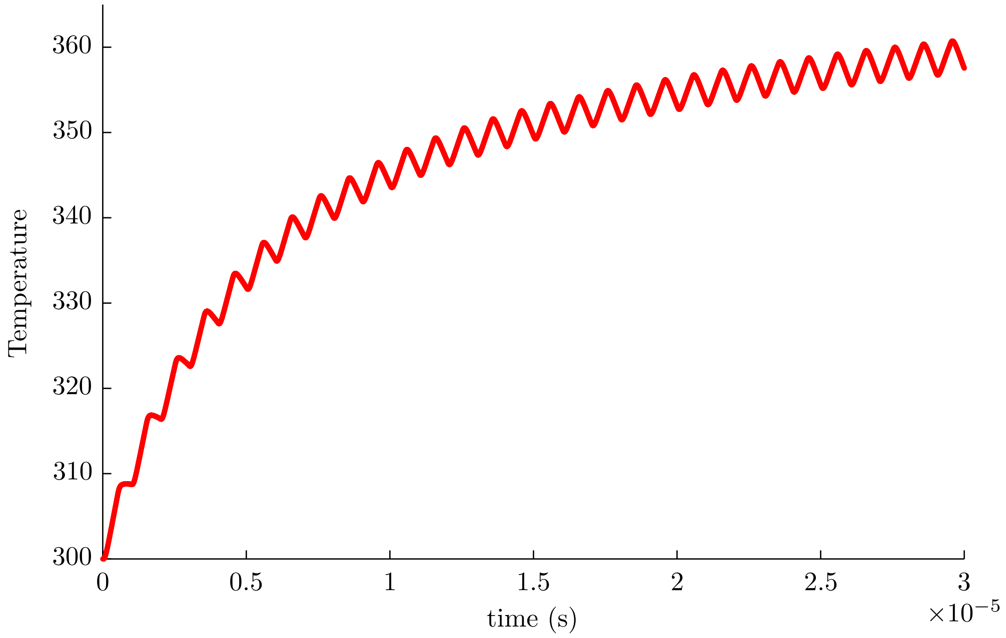

Figure 3.10: Simulation result of a bubble under standard conditions with heptane oil.

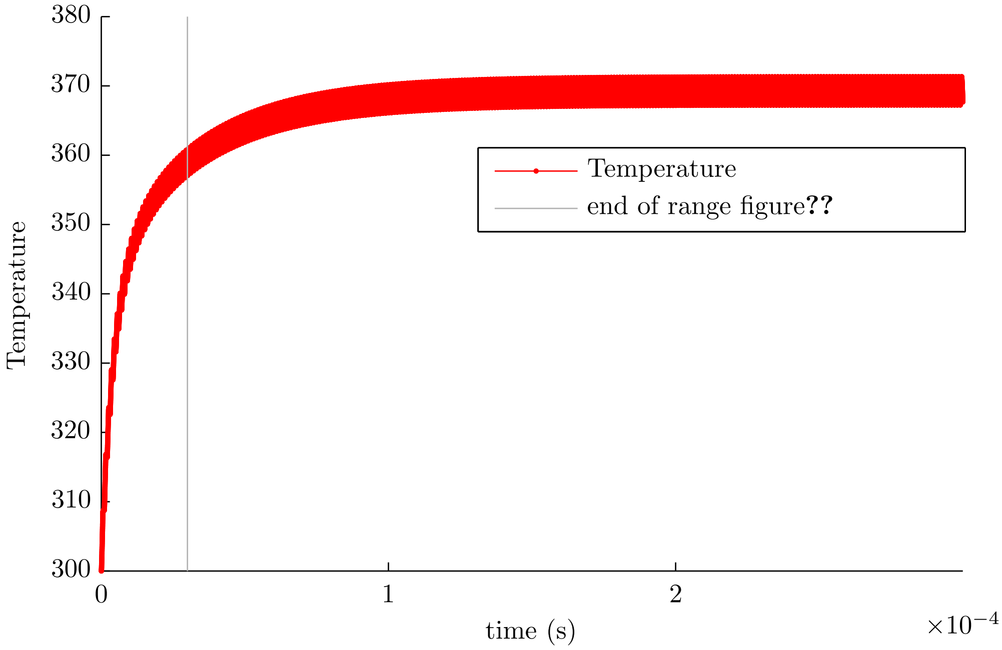

Figure 3.11: Simular to Figure 3.10 but for a longer time frame.

predicted by the linearization of the simplified model because the transfer function was of a third order.

In Figure 3.11 it can be seen that the temperature converges to a value of approximately 371 K. When the simulation is run for even longer it can be seen that this value changes less then 10^{-5} K (3×10^{-6} %) from simulation time 1 ms to 3 ms where this small number is the accuracy of the simulation. This shows that there is no significant error for each time step that builds up on the simulation result. Furthermore, a converging temperature is the expected scenario.

Figures 3.12 and 3.13 show the resonance curves in several different scenarios. The conditions are the standard conditions as described for Figures 3.7, 3.8 and 3.10 in case of the red line. The black line describes the very same bubble in a bath of human body temperature. From these graphs it can be seen that bubbles with a very narrow size distribution around 3 µm in radius would give the optimal signal. There is a slightly higher response at body temperature. This difference is expected to be a result of the temperature dependent water viscosity.

In Figure 3.15 the resonance curves are shown again but with a larger range of initial bubble sizes. The resonance curve of a free bubble under 50 kPa ultrasound insonation, obtained from a separate program, is added. For this free bubble the resonance peak is much less sharp and monodispersity

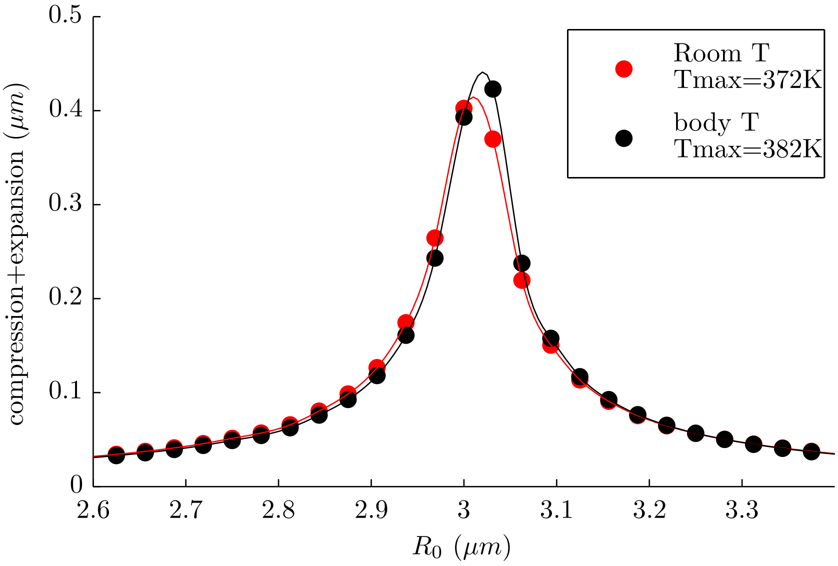

Figure 3.12: The resonance curve for oil bubbles under standard conditions. The red data is in a bath of room temperature and the black data is for a bath of human body temperature. The line between the data points is a spline interpolation. compression+expansion is defined as the peak to peak oscillation distance.

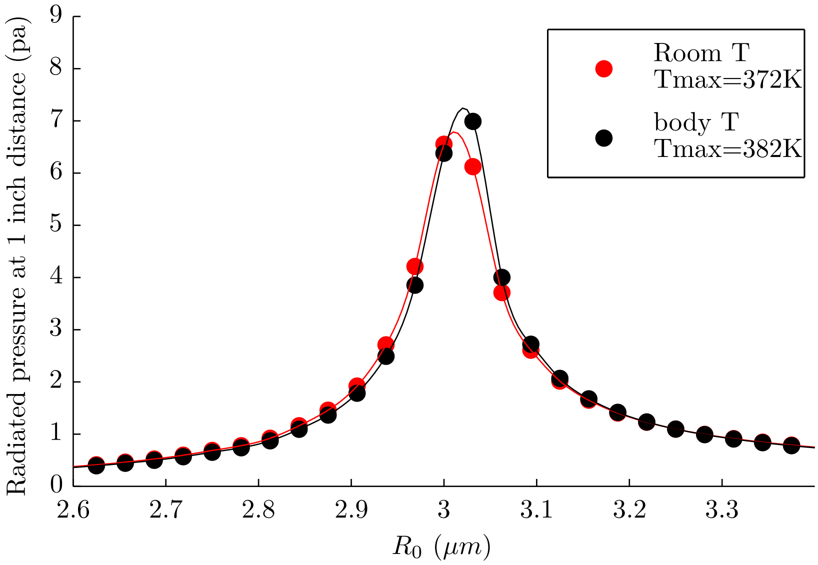

Figure 3.13: The resonance curve in terms of radiated pressure for oil bubbles under standard conditions. The red data is in a bath of room temperature and the black data is for a bath of human body temperature. The line between the data points is a spline interpolation.

of bubble sizes is thus less critical than for the heptane bubble. The free bubble curve resembles the resonance curve that is found for a bubble in standard conditions with triacetin oil. This curve can be found in Figures 3.16 and 3.17.

In 3.14 the maximum temperature for each radius of the curves shown in Figures 3.12 and 3.13, is plotted. A third curve is added to show that less dye, or similarly, less laser power is needed to reach boiling temperatures in the human body. For this graph the absolute maximum temperature is used, being the maximum temperature in the last period of laser oscillations. In case the average temperature during the last laser period would be used instead, the graph would look almost identical but slightly shifted towards lower temperatures.

In Figure 3.19 the fast Fourier transform of the simulated radius time curve of a bubble in resonance can be seen. This curve is for a bubble oscillating around equilibrium and it can be seen that there are higher harmonics. The bubble is driven at 1 MHz and smaller peaks are found at the second, third and fourth harmonic. In Figure 3.20 the results for the simplified model can be found. In this figure the green line again shows peaks at higher harmonics. The red line is the Fourier transform of the resonance time curve for a bubble with twice the resonance size and the blue line is for a bubble half the resonance size. All curves are normalized with the

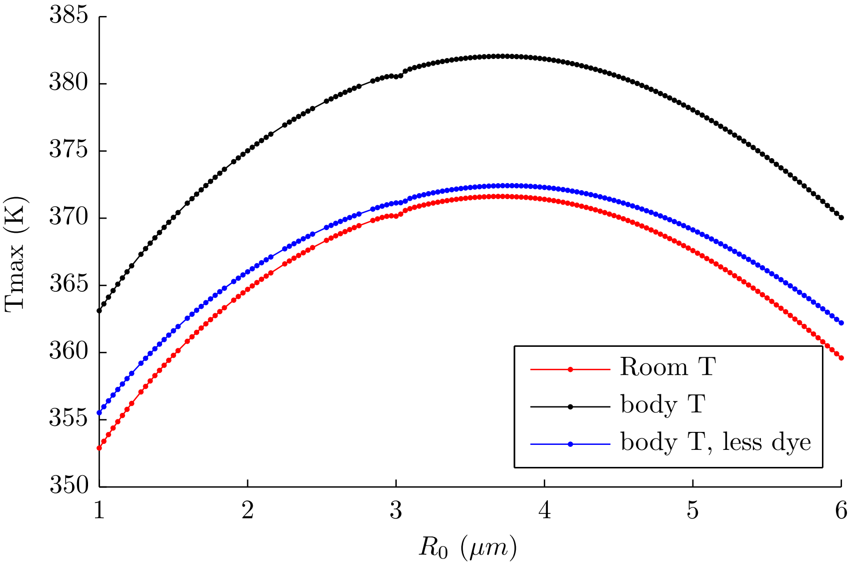

Figure 3.14: The maximum temperature reached during simulation. Each data point is a complete simulation and at no point does the red or blue line exceed the boiling point of water. The red and black line correspond to the red in black line in Figure 3.13 and 3.12, the blue line is in human body temperature bath but with a lower absorption coefficient of the dye.

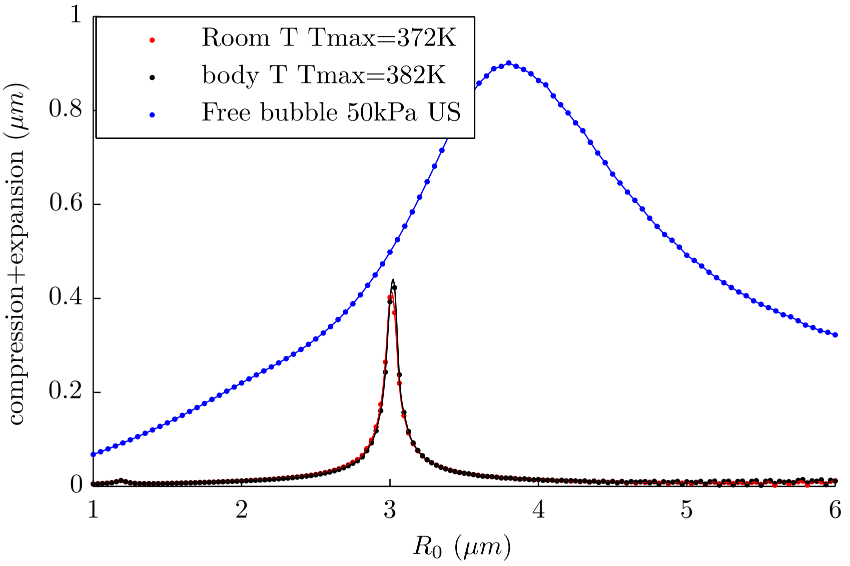

Figure 3.15: Resonance curve of a free bubble under 50 kPa ultrasound insonation (blue line)and the red and blue line are oil bubbles under standard conditions but the black one is in a human body temperature bath.

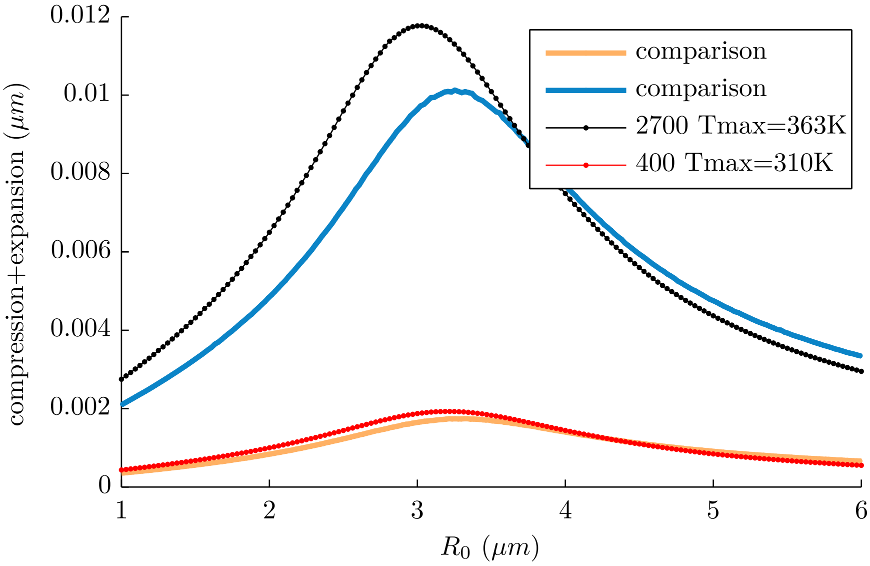

Figure 3.16: The resonance curves for a triacetin oil bubble under standard conditions. The high lines have an absorption coefficient similar to that used with heptane, and the low line has an absorption coefficient which is maximum for triacetin. Blue and orange line are comparisons to simplified model according to 3.20

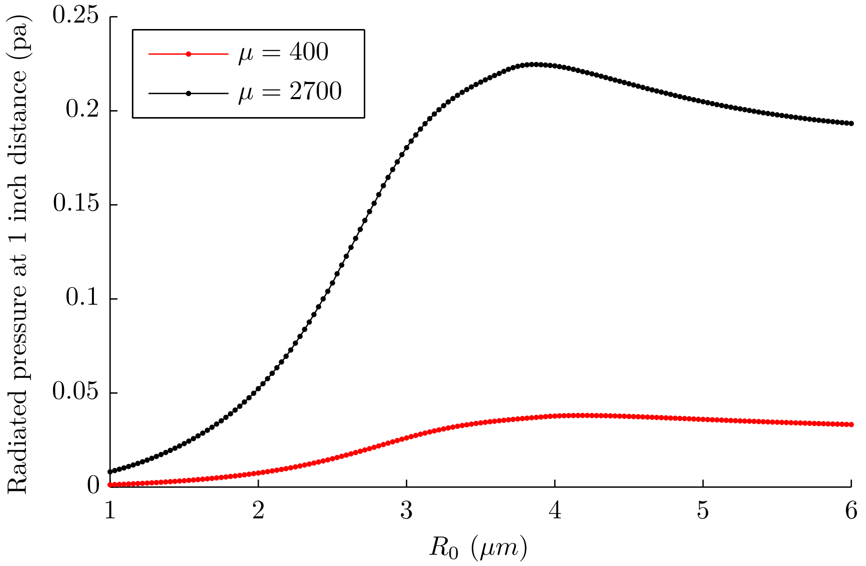

Figure 3.17: The radiated pressure curves for a triacetin oil bubble under standard conditions. The high lines have an absorption coefficient similar to that used with heptane, and the low line has an absorption coefficient which is maximum for triacetin.

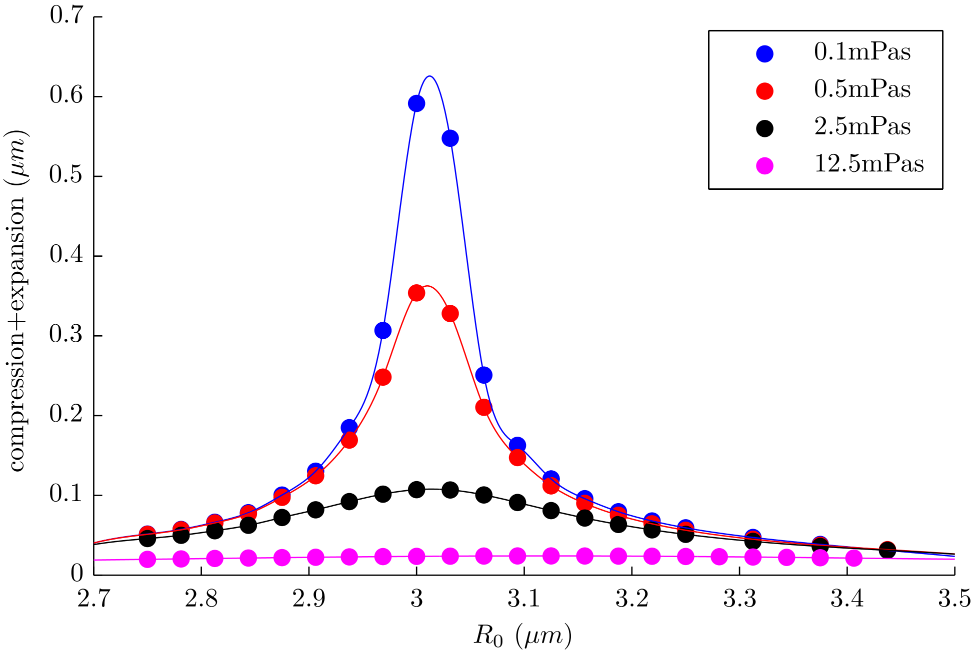

Figure 3.18: Resonance curves for different oil viscosities.

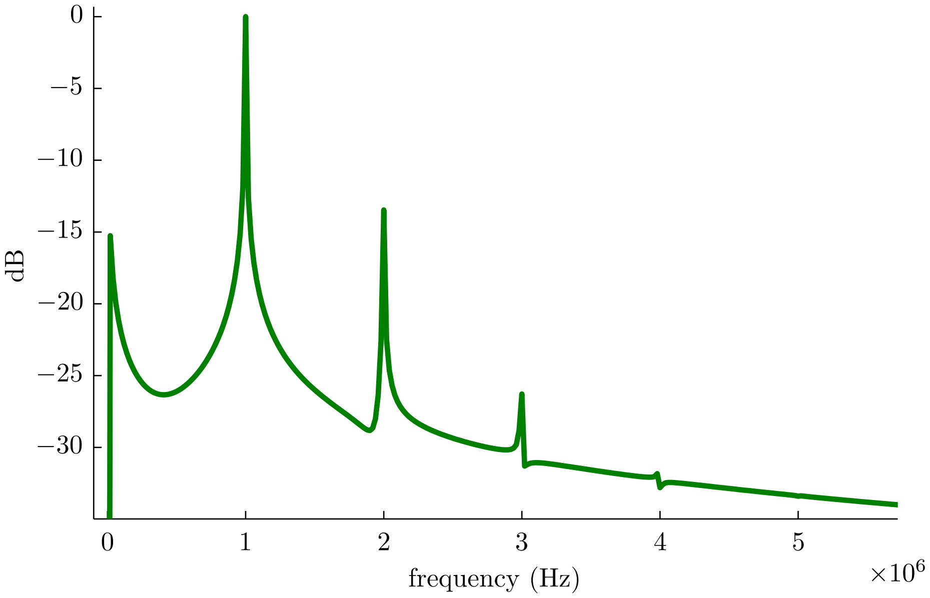

Figure 3.19: The fast Fourier transform for a bubble under standard conditions with square wave laser modulation in resonance according to the full simulation.

maximum of the green line.

In Figures 3.16 and 3.17 the resonance curves can be seen for a bubble with a 1 µm thick triacetin oil layer and further standard conditions. Two curves are shown, one with an absorption coefficient similar to the one used for heptane (2700 m^{-1}) and one with an absorption coefficient that would be the practical upper limit for triacetin because not more dye can be dissolved in it (400 m^{-1}). The response, both in radial oscillation and in radiated pressure is much lower than for the heptane-covered bubble. In case of the high absorption coefficient the temperature does increase almost as much as for the heptane bubble. The only parameter that changes more than an order of magnitude between triacetin and heptane is the used oil viscosity: 17 mPa s for triacetin and 0.386 mPa s for heptane. To investigate the influence of oil viscosity, resonance curves were plotted in Figure 3.18 for several oil viscosities leaving all other parameters unchanged (standard conditions). It is clear that oil viscosity has a huge influence on response within the range of viscosities that are common for oils.

This simulation result can be compared to the simplified model made in the previous section. In order to do this, (3.20) was solved in Matlab using the standard function `ode113`. In Figure 3.16 the resulting lines are plotted in blue and orange. They match relatively well. This simplified model will

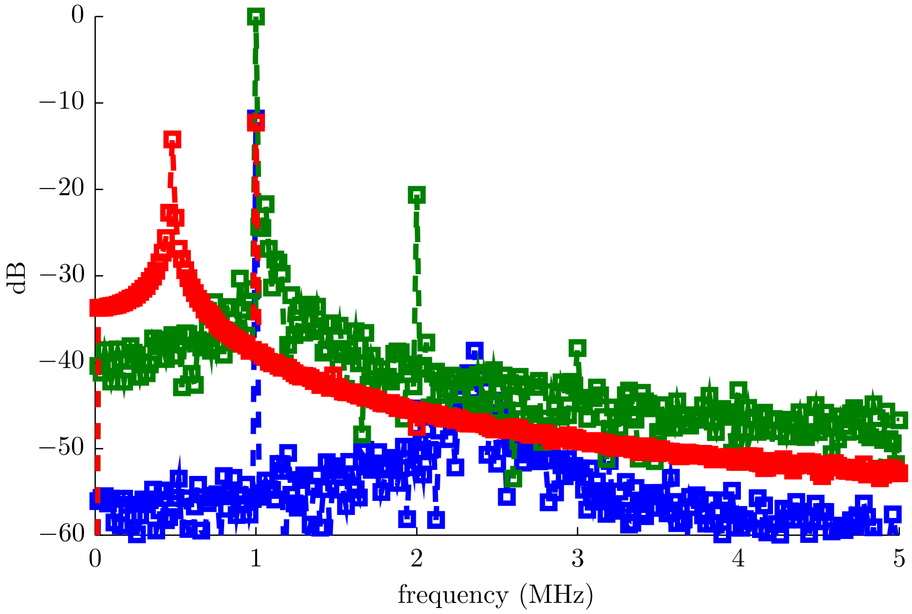

Figure 3.20: The fast Fourier transform for a bubble under standard conditions with square wave laser modulation according to the simplified model. The green line is for a bubble of resonance size, the red line has twice the resonance size and the blue line is for a bubble half the resonance size.

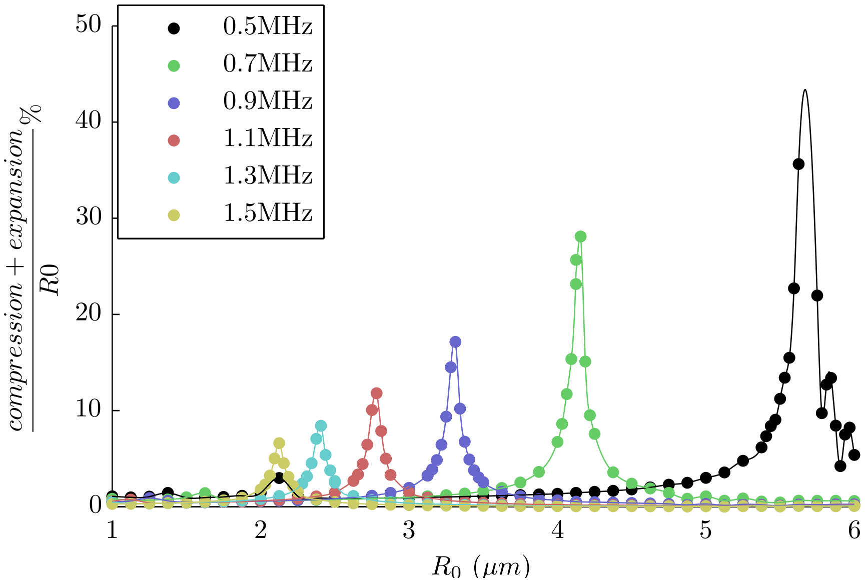

Figure 3.21: The resonance curves for heptane oil bubbles at different laser oscillation frequencies.

be further analyzed to investigate its accuracy and limitations.

In Figures 3.21 and 3.22 the resonance curves for different laser modulation frequencies can be seen. As would be expected, bigger bubbles resonate at lower frequencies. Another thing to note in this figure is the smaller peak just over 2 µm for a 0.5 MHz laser modulation. The radius- time curve that corresponds to this small peak is plotted in Figure 3.23. This indicates a higher harmonic at three times the resonance frequency.

In Figure 3.24 two resonance curves are shown. All parameters are the same but for the black curve the laser is modulated as a square wave and for the red curve the laser is modulated as a sine wave. A sine wave can be considered more basic because all wave shapes are theoretically made up of a combination of sine waves. The curves show mainly the same behavior showing that the simulated results are mostly independent of the shape of the laser modulation. However, the small peak for the square wave modulation at approximately 1.2 µm is not present for the sine wave. This is to be expected because a square wave is primarily made up of a sine wave at its modulation frequency but the second highest component is a frequency three times that. This frequency is not present in a pure sine wave. Furthermore, the resonance peak is lower for a sine wave despite the same amount of power. An hypothesis of why this is so is the following: After the start-up effects are over and the bubble oscillates around the equilibrium radius, all that matters is the deviation from average powers. In case of a square wave, the power is always maximally far away from the average power and in case of a

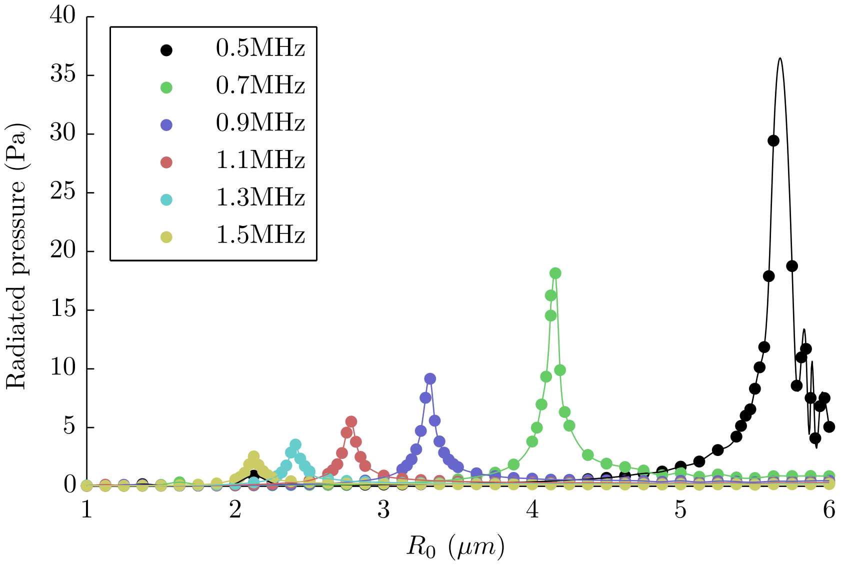

Figure 3.22: Simplified model comparison to Figure 3.21. The resonance curves for heptane oil bubbles at different laser oscillation frequencies.

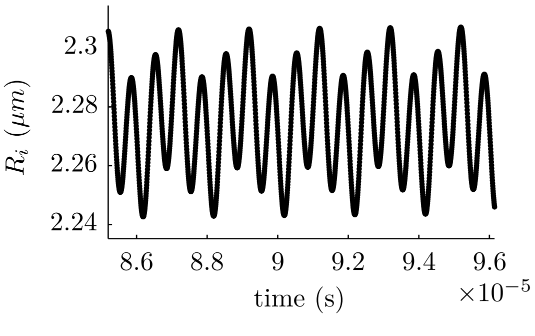

Figure 3.23: The subharmonic behavior found at the small peak of the 0.5 MHz line just over a initial radius of 2 µm in Figure 3.21.

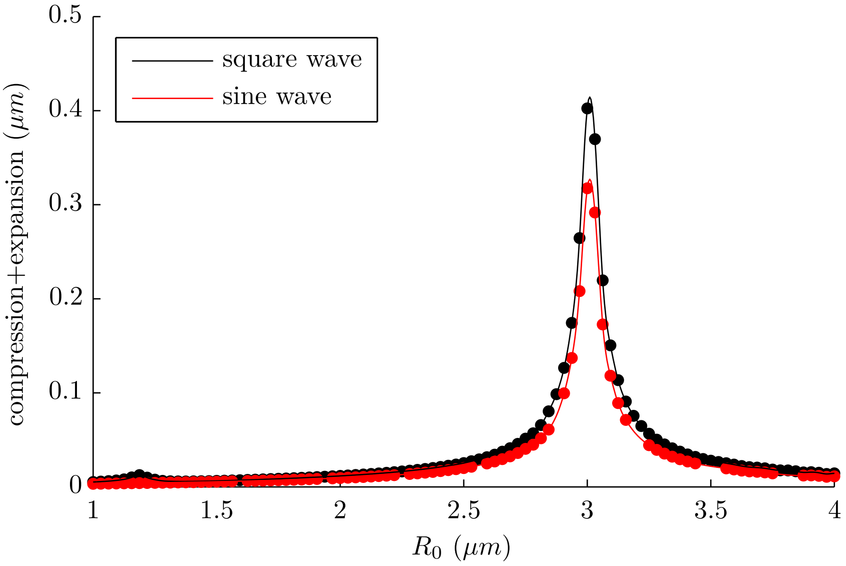

Figure 3.24: The resonance curves for a laser modulated as a sine wave and a laser modulated as a square wave. A higher harmonic at a third of the resonant radius is found for the square wave but not for the sine wave. Also, the response for the square wave is slightly higher which can be expected from the fact that, when it heats, it heats as much as possible and when it cools down, it cools as much as possible.

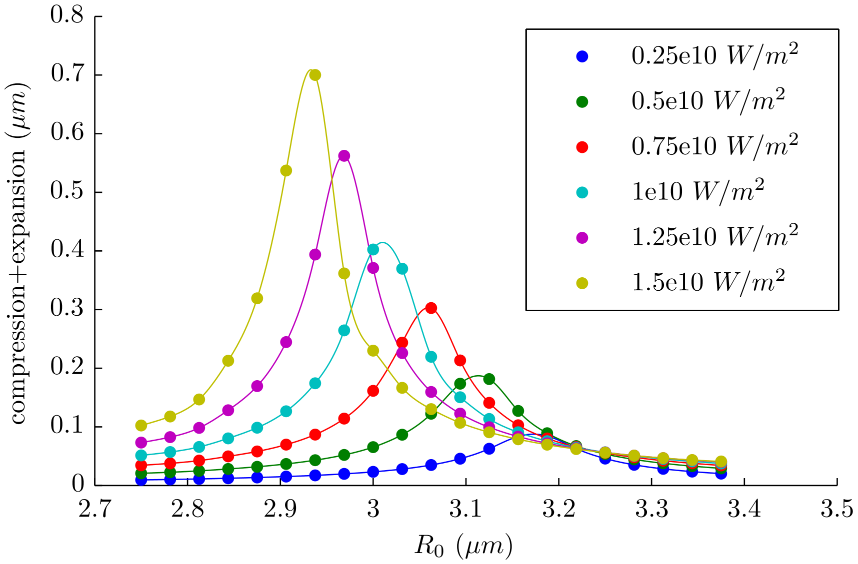

Figure 3.25: The resonance curves for a heptane oil bubble for different laser intensities.

sine modulation it only reaches this for two points in time for each period. This is most intuitive when looking at the cooling phase. In case of a sine wave the laser will mostly be shining but in case of the square wave it will be off all the time allowing the bubble to cool further.

In Figure 3.25 the resonance curves for different laser powers can be seen. It can clearly be seen that the resonance peak goes to smaller radii for higher laser powers. this is what is expected because, as can be seen in Figures 3.10 and 3.11, the bubble temperature oscillates around a temperature that is higher than the starting temperature. This causes the radius to oscillate around a bigger value than the starting value. In other words, the equilibrium radius resonance peak remains the same for all laser powers. This can be seen in Figure 3.27. Because the difference between starting radius and equilibrium radius gets larger for higher laser powers, the initial radius resonance peak gets lower as shown in Figure 3.25.

Figure 3.25 is compared to the simplified model again and the plotted result can be found in Figure 3.26. The similarity of the full simulation and the simplified model is convincing. The behavior and the amplitude is very similar but the simplified model is shifted by approximately 0.1 µm

In Figure 3.28 the simulated resonance curves are shown for different oil layer thicknesses in case of heptane. Figure 3.30 show this for triacetin (standard conditions). Figures 3.29 and 3.31 show the result plotted for the simplified model. Again there is a shift in the resonance frequency which seems to be bigger for thicker oil layers but other than that the similarity,

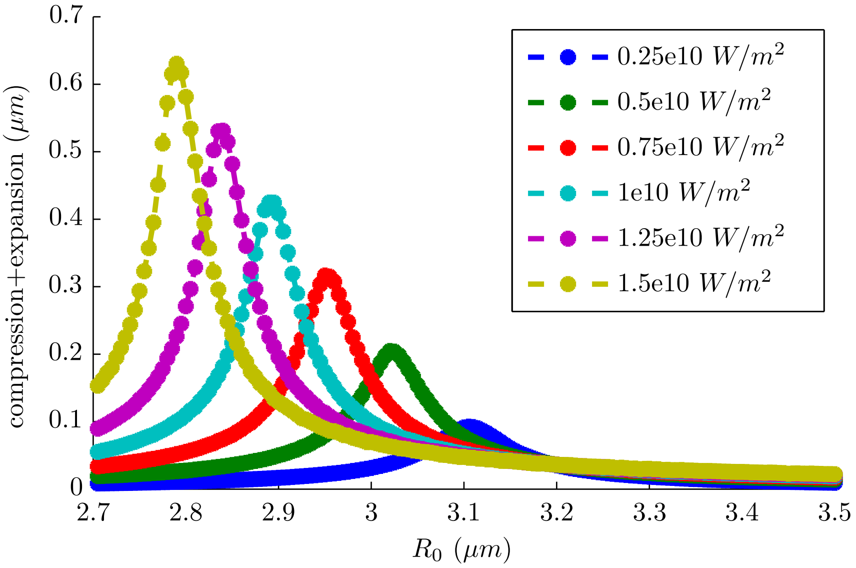

Figure 3.26: The resonance curves for a heptane oil bubble for different laser intensities according to the simplified model as a comparison to Figure 3.25.

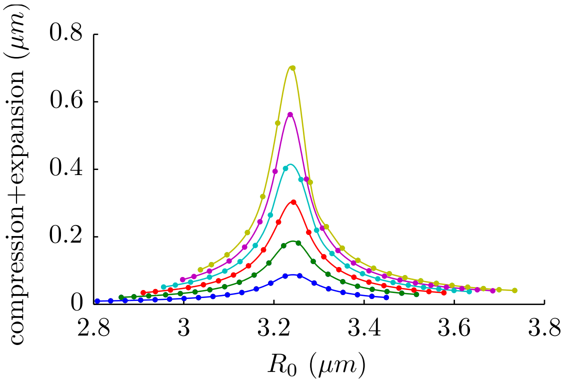

Figure 3.27: Same as Figure 3.25 But the x-axis is the equilibrium radius. As expected, all curves have their peak at the same equilibrium radius.

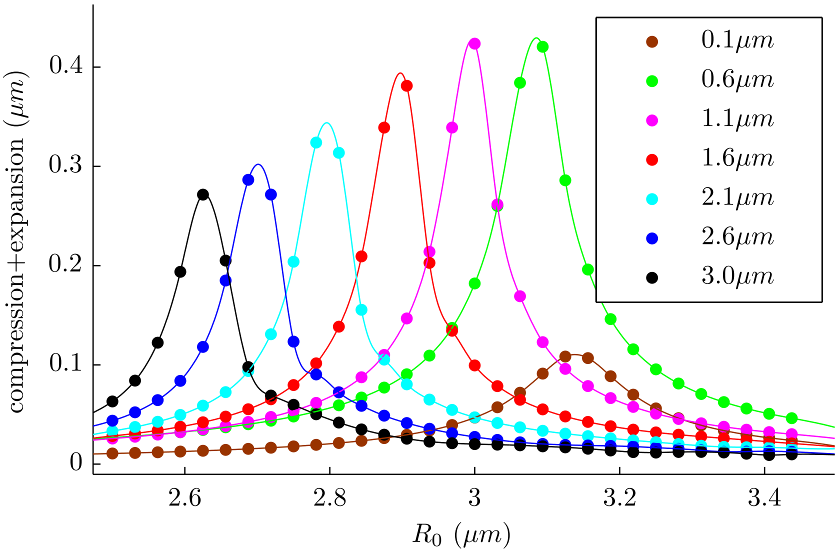

Figure 3.28: Resonance curves for different heptane oil layer thicknesses.

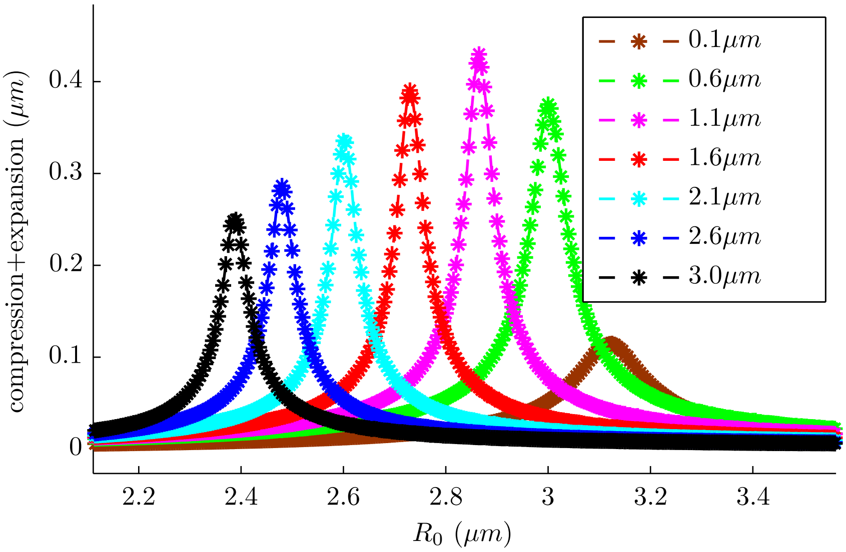

Figure 3.29: Resonance curves for different heptane oil layer thicknesses according to the simplified model. This is a comparison to Figure 3.28.

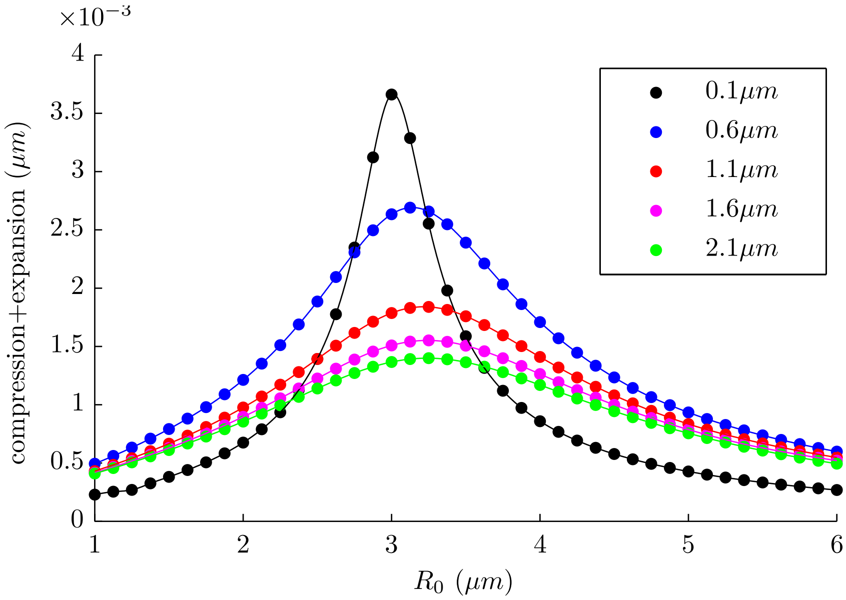

Figure 3.30: Resonance curves for different triacetin oil layer thicknesses.

especially the behavior, is very convincing. As predicted in the linearization of the simplified model (equation 3.58), there is an optimum for heptane oil layer thicknesses. A 0.1 µm thick oil layer has a lower response than a 1.1 µm oil layer but much bigger oil layers give a lower response again due to damping. For triacetin it was mentioned in the linearization that is should not have a maximum response which again can be seen; the smaller the triacetin oil layer the higher the response. Of course there will be a point where the response will be decreasing if the oil layer is further decreased. However, this behavior at very thin oil layers is not present the scope of our theory.

3.8 Conclusions

The simulation gives clear results that can contribute to making optimal choices for contrast agent dimensions and compositions. The simplified model and the linearization of this model were introduced for a better understanding and both agree well with the full numerical simulation. The results of plotting the simplified solution are in fact in such good agreement that this could be a better method to find the optimal contrast agent dimensions and composition because the computation time is in the order of 1000 times faster.

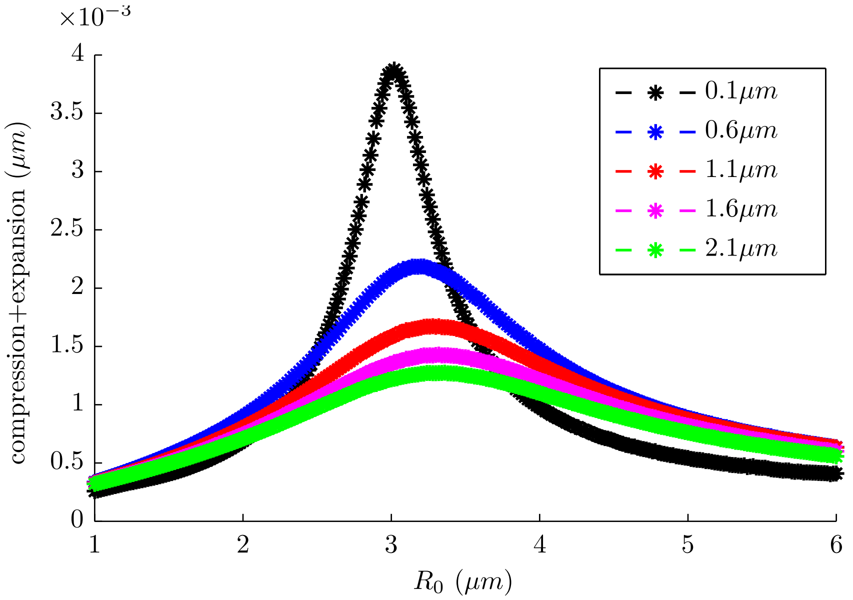

Figure 3.31: Resonance curves for different triacetin oil layer thicknesses according to the simplified model. This is a comparison to Figure 3.30.

3.9 Discussion of validity model

The simulation has shown clear dependencies of different parameters and conclusions about which bubble to choose can be made based on them. However, the simulation has some strong assumptions that must be considered. The first is that the influence of surfactants and phospholipid coating has not been taken into account. Not much is known about the effect of a phospholipid coating at a water-oil interface and therefore it cannot be part of the simulation at this point. However, as mentioned by Zhang and Huynh, surfactants can have a great influence on surface tension [15, 16]. In Figure 3.32 the same simulation, but for two different oil-water interfacial tensions, is shown. It is also known that a phospholipid coating on its own causes some additional damping [17]. An estimation of this influence would be difficult to make but it could potentially cause a difference between simulated result and practice.

Another point that could cause a difference between simulated result and practice is that the viscosity of oil is temperature dependent. This is not taken into account in the simulation because not enough information was available on this. This could of course be measured and then put in the simulation. This is very much recommended because Figure 3.18 clearly shows the great influence of the oil viscosity. The simulation assumed oil viscosity at room temperature but in reality the viscosity around boiling point (373 K) would be a better measure. The simulation would probably

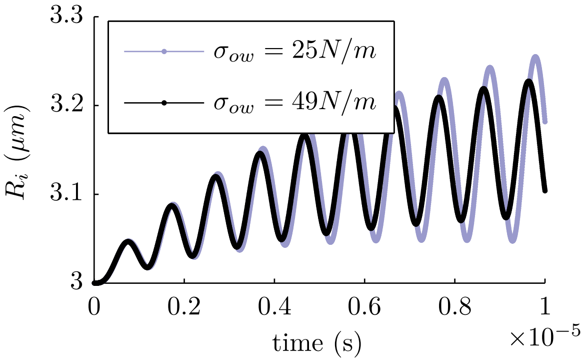

Figure 3.32: Two example runs for the standard oil-water interfacial tension and for half of this value. The interfacial tension could change due to surfactants but this is not taken into account in the simulation. This figure shows that this could mean a less accurate result.

give much higher radiated pressures if the temperature dependence of oil was taken into account.

Chapter 4

Towards experimental validation

The simulations have shown that an oil-coated bubble can be a good contrast agent, especially when the viscosity of the oil is low. The next step would be to actually create these bubbles. Although a stable and usable bubble could not be produced in significant amounts, this chapter will show some achievements as well as the main difficulties encountered in the process.

Earlier research shows that microbubbles with an oil layer can be produced [18–20] and the most monodispersed results come from flow-focusing devices. A lot of research has been performed to create mono-dispersed, phospholipid-coated microbubbles in microfluidic devices [21–27]. An attempt was made to produce monodispersed microbubbles with an oil layer by using a method much like that of Shih, 2013 [19]. In this paper traicetin oil was used. We also used this oil but also tried other less viscous oils.

4.1 Chip design

The most important step in the production of microbubbles is flow-focusing. An example of simple flow-focusing is shown in Figure 4.1. As described by Stride and Edirisinghe [28], *"the essential feature of the device is an orifice at which a column of gas impinges upon a liquid flow and is focused into a jet. Subsequently, at a certain distance from the orifice, the gas-liquid interface becomes unstable and bubbles are formed by a "pinch-off" process."*. The device designs we used include an extra oil channel to obtain an oil layer around the pinching bubble. For this the principle remains the same but the pinched jet will have an oil layer surrounding it. Often the gas bubble is pinched off inside the oil layer while the oil pinches off later. Examples of this can be seen in Figure 4.2 and more clearly in Figure 4.3.

The design of the chip can be seen in Figure 4.4. There are two different designs, One, later referred to as the 'single-pinch design' is very much like

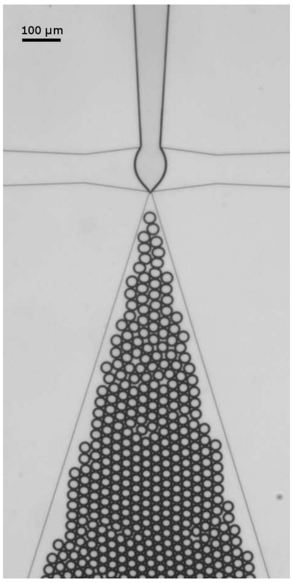

Figure 4.1: A more simple microfluidic device producing monodispersed bubbles without oil.

the chip described in the paper of Shih (2013) [19] but the exact dimensions are sometimes different. For example, the orifice in our design is 10 µm wide where Shih used a 5 µm wide orifice. This 10 µm orifice was chosen in the first generation designs of the oil bubble devices and seemed to work well. In the single-pinch design chip both the oil jet and the gas jet pinch after the orifice (Figure 4.2). The second design is later referred to as the 'double-pinch design'. In this design the air jet is pinched by the flow of oil creating bubbles in an oil jet. The oil jet is later pinched at the orifice in order to create the oil-covered bubbles.

The Reynolds number in the chip is in the order of 1 assuming the smallest length scale of 10 µm, speeds around $0.1\,\mathrm{ms}^{-1}$ and a kinematic viscosity of water $10^{-6}\,\mathrm{m}^2\mathrm{s}^{-1}$. From this it can be concluded that the flow is always laminar within the chip.

4.2 Materials and production

The microfluidic devices are produced according to a standard procedure as described in the Master thesis of M.P. Kok, quite similar to the method described by Hong et al and Shih et al. [19, 29, 30]. A reusable mold is first produced in a cleanroom and single-use microfluidic devices are made with poly(dimethylsiloxane) (PDMS) attached to a glass microscope slide in a time frame of two to three hours. The result is a transparent chip allowing for real time visualization of the processes.

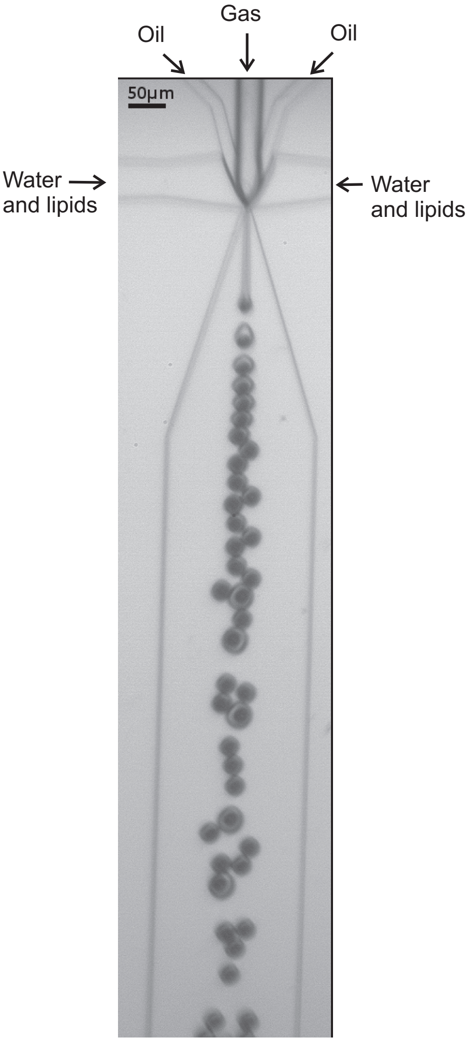

Figure 4.2: A microfluidic device producing monodispersed bubbles surrounded by triacetin oil and coated with DSPC and DSPE-PEG2000 lipids. This is a single-pinch chip design. The picture shows the different inlets.

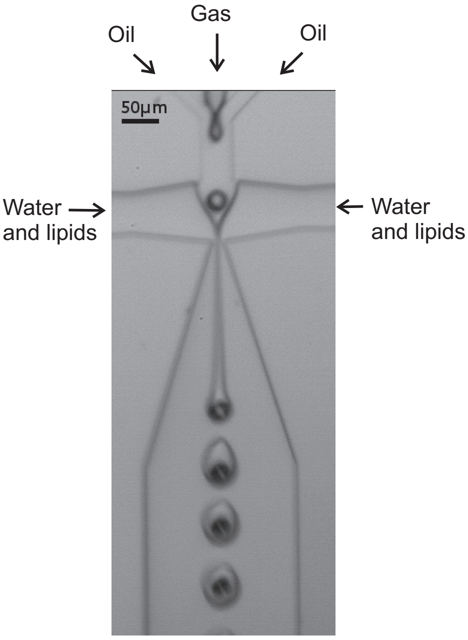

Figure 4.3: A microfluidic device producing bubbles surrounded by triacetin oil and coated with phospholipids (Dreft in this example). This is a double-pinch chip design. The picture describes all different inlets

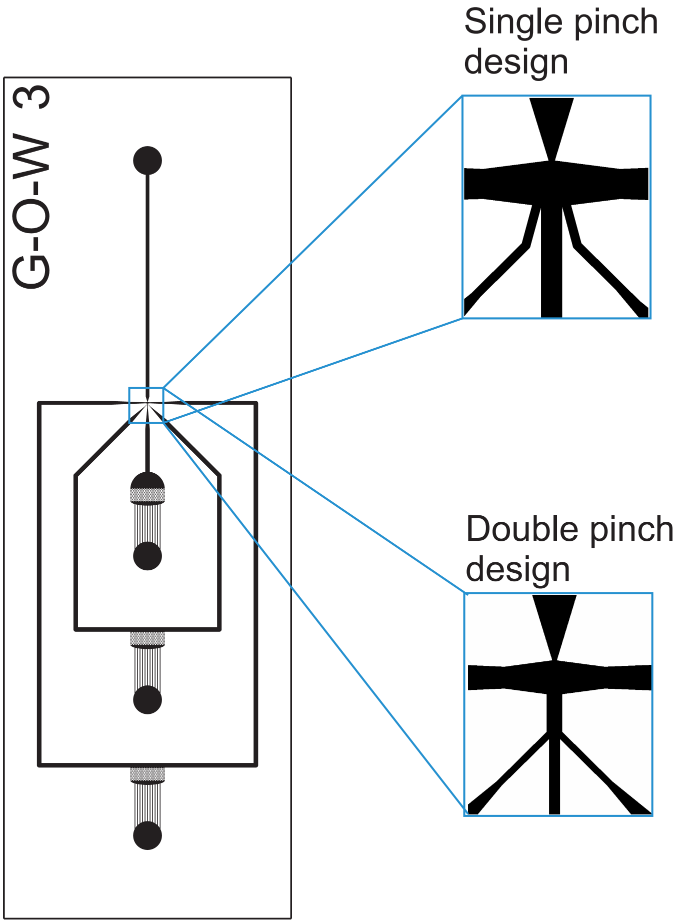

Figure 4.4: The chip design

4.2.1 Pressurizing the device

When the chip is first connected to the lipid solution, the oil and the gas, the lipid solution must first be put in all channels of the chip in order to keep the hydrophilic behavior of the channel walls that was created by the plasma cleaning and bonding. After this, just giving high gas pressures or high oil flow rates would result in the entire chip being filled with gas or oil, respectively. If oil gets in all channels it is difficult to remove this. The lipid solution must flow through these channels for a long time to wash out the oil. In case of a gas channel the oil stays in there for the entire duration of the experiment. The best way to reach a stable production stage is by first, choosing a low water flow rate and slowly increasing the gas pressure until nice monodispersed bubbles are produced without an oil layer. Then, to increase the oil flow rate without destabilizing this production rate. While doing this, the gas pressure and water flow rate probably have to be increased; Starting with high flow rates of water (i.e. lipid solution) before the oil flow has started and before the gas pressure is high may result in water flowing in the oil and gas tubing and it would take a lot of time to undo this. Going through this procedure of starting with low flow rate and steadily going up takes approximately 30 to 60 minutes. The device is considered pressurized when all three phases are going through the outlet. When this state is reached one can start looking for a combination of flow rates that gives monodispersed oil-covered bubbles.

4.3 Setup

The production of microbubbles is recorded through an upright Olympus microscope, through the PDMS layer with a Photron fastcam SA7 type 30K-M2 camera or a Fastcam SA-X2 type 1080K-M4 camera. An Olympus ILP-1 lightsource is used for illumination. Two syringe pumps are used to control the flow of oil and lipid solution, these were Harvard apparatus PHD 2000 infuse/withdraw. For the oil a 5 mL glass syringe is used and for the water a 10 mL plastic syringe is used. Working with a glass syringe for the oil is required in case of heptane or decane because these oils may dissolve plastics. The water and oil then go through 30 cm long PEEK tubing with a 0.040 inch inner diameter. The gas flow is controled with a Omega Engineering inc. pressure controller. The gas is sent through a 30 cm long 0.020 inch PEEK tube. The PEEK tubes are connected to the PDMS chip via precision tips (18GA PPS .032X.5” GRN 50PC) from Nordson EFD.

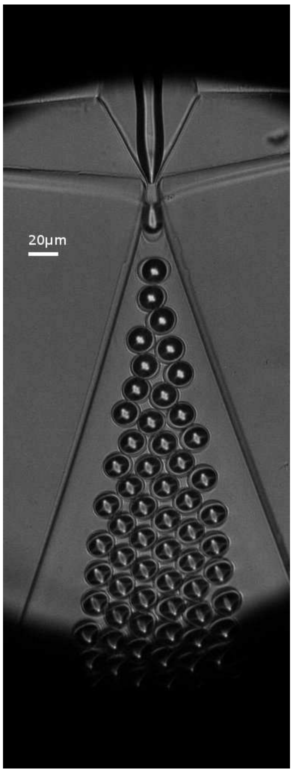

Figure 4.5: Single pinch design chip with high production rate; heptane covered bubbles.

4.4 Results

The single-pinch design of the oil bubble chip was capable of producing monodispersed, triacetin oil covered, DSPC, DSPE-PEG2000-coated air bubbles for several hours non-stop as shown in Figure 4.2. This production stage was relatively easy to reproduce. Also, high production rates (>50 000 bubbles per second) have been achieved with the single-pinch design using low viscosity heptane (386 µPa s) as the oil and 5 % Dreft desolved in the water as a surfactant. The results with heptane were very difficult to reproduce. The resulting bubbles in both cases were unstable in time meaning that most of the bubbles had already disappeared or coalesced in less than one minute.

The desirable result would have been a high production rate with low viscosity heptane oil, stable for hours and easily reproducible. Each of these points has been accomplished but unfortunately not all together.

4.5 Summary

This chapter shows that the production of oil and phospholipid coated bubbles was successful. However, the produced bubbles were highly unstable making them unusable for its purpose: to function as contrast agents in continuous wave photoactoustic imaging. Furthermore, none of the oils that were used are suitable for this process. Triacetin has a too high viscosity and heptane and decane dissolve the PDMS chip. A new low-viscosity oil must be found.

4.6 Discussion

Here we describe the main difficulties in producing the bubbles and suggests possible solutions.

Most of the experiments have been done with heptane oil because this promised to result in a better contrast agent. The biggest problem with heptane however, is that is damages the PDMS. After approximately 90 minutes, the PDMS chip has swollen and in the case where a red dye was added to the heptane, the whole chip would be colored in red. This indicates that heptane gets absorbed by the PDMS and possibly the swelling changes the dimensions of the chip. Also, after 90 minutes the bonding between the PDMS and the glass would snap and the chip would no longer be usable. 90 minutes seems like a long time but often this was not enough to reach a continuous monodisperse bubble producing stage. One of the reasons for this is that approximately 30 to 60 minutes is needed to pressurize the device as mentioned before, but also in a pressurized chip it can be difficult to find a regime that produces stable bubbles.

Figure 4.6 shows an example of what happens at too high oil flow rates. When the oil flow rate is too low no more oil gets through the orifice and the bubbles have no oil layer. Sometimes the problem is less easy to understand and the oil and water go through the orifice one after another instead of together producing oil droplets and air bubbles, as shown in the left picture in Figure 4.6.

In an attempt to find an oil that would not break the chip quickly but would still have a low viscosity, decane was used. Decane damaged the PDMS slightly less than heptane but similar problems persisted. Therefore, for future designs a new oil must be found that does not damage PDMS, but that does have a low viscosity.

When choosing this new oil, part of the consideration should be to see if it is energetically favorable for air to remain in the oil layer. Figure 4.7 shows that air bubbles often leave the oil layer without an obvious flow or force in that direction.

Despite all difficulties, sometimes oil-covered bubbles of the right size were produced but when placed under a microscope, it could be seen that the air dissolved rapidly. Unexpectedly this was also the case when using the same oil and the same lipids, in the same ratio and amount as mentioned in the literature to give stable bubbles [19]. In an attempt to fix this problem, the lipid solution and the oil were air saturated by stirring them overnight but this did not seem to have a significant influence.

An interesting point is that the chips were more likely to go to a nicely producing state when a 5 % Dreft solution was used instead of the DSPC, DSPE-PEG2000 solution. One reason for this could be that the concentration of these lipids is much lower (0.05 %) and therefore coating the bubbles could take much longer. From literature it is well known that coating microbubbles produced in a flow-focusing device is challenging [27, 31]. The strong interaction between the phospholipid molecules make them an excellent coating material to stabilize bubbles for days. However, the strong interactive forces make it also hard to break apart the micelles and liposomes that phospholipids form naturally when they are in a water solution. It is therefore likely that the coating process of bubbles in a flow-focusing device is challenging because there is not a lot of shear energy to break apart the micelles and liposomes to let them form a coating around the bubble. When the bubbles are not coated right after they are ejected from the orifice they will coalesce downstream. One way to overcome the coalescence problem is to simply increase the possibility of the bubble to come into contact with micelles and liposomes by increasing the phospholipid concentration in the water solution. Another possible solution could be the addition of extra surfactant (Pluronic F68) to coat the bubble right after it is produced [19]. This requires however that the pluronic molecules at the air-water interface are later on replaced by phospholipds through self-assembly. We don't think this is likely to happen and this can be the cause for the short term stability of the bubbles produced by Shih et al..

Moreover, the solvability of the lipids can be increased by increasing the liquid temperature. In a lipid solution micelles and liposomes are formed which first have to dissemble before the phospholipids can form a coating around the oil bubble. By heating the lipid solution above the glass transition temperature the lipids are more free and therefore more readily available. Both adding more lipids and heating them could also potentially make the bubbles more stable in time. Finally, one could search for different lipids that possibly are better suited for the oil bubble since the lipid formulation being used in this study is a lipid formulation generally used to coat gas microbubbles [25, 32]. One could also vary the main lipid to emulsifier ratios which possibly has an influence on the oil bubble stability [25].

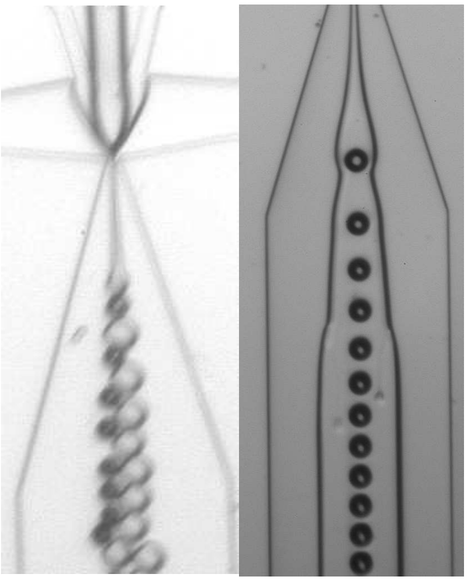

Figure 4.6: Badly working chip. On the left the air and the oil go through the orifice on after another instead of together and on the right the oil flowrate is so high that all bubbles end up in one big oil layer.

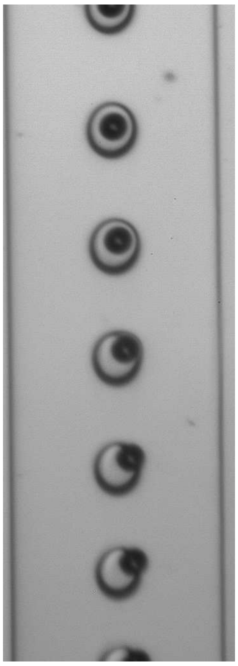

Figure 4.7: Triacetin covered bubbles in a low speed flow. The air bubbles leave the triacetin layer.

Appendix A

Standard conditions

variable	**unit**	**heptane**	**triacetin**
Thermal conductivity oil λ_o	$\mathrm{Wm^{-1}\,K^{-1}}$	0.13	0.17
Thermal conductivity water λ_w	$\mathrm{Wm^{-1}\,K^{-1}}$	0.61	0.61
Thermal conductivity gas λ_g	$\mathrm{Wm^{-1}\,K^{-1}}$	0.026	0.026
Density oil ρ_o	$\mathrm{kgm^{-3}}$	678	1.15×10^3
Density water ρ_w	$\mathrm{kgm^{-3}}$	10^3	10^3
Heat capacity water cp_w	$\mathrm{Jkg^{-1}\,K^{-1}}$	4.19×10^3	4.19×10^3
Heat capacity gas cp_g	$\mathrm{Jkg^{-1}\,K^{-1}}$	1.04×10^3	1.04×10^3
Heat capacity oil cp_o	$\mathrm{Jkg^{-1}\,K^{-1}}$	2.25×10^3	1.76×10^3
Molar mass	$\mathrm{kgmol^{-1}}$	28×10^{-3}	28×10^{-3}
Surface tension oil σ_o	$\mathrm{Nm^{-1}}$	20×10^{-3}	36.5×10^{-3}
Surface tension oil-water σ_{ow}	$\mathrm{Nm^{-1}}$	48.95×10^{-3}	4.72×10^{-3}
Surface tension water σ_w	$\mathrm{Nm^{-1}}$	72.8×10^{-3}	72.8×10^{-3}
Room temperature	K	300	300
Oil viscosity (μ_o)	Pa s	386×10^{-6}	17×10^{-3}
Absorption coefficient	$\mathrm{m^{-1}}$	2700	400
Laser intensity	$\mathrm{Wm^{-2}}$	10^{10}	10^{10}

variable	**unit**	**value**
Initial bubble radius Ri	µm	3.0
Initial bubble thickness	µm	1.0
Room temperature T_{room}	K	300
Maximum simulation time	s	10^{-4}
laser frequency	Hz	10^6
inner, initial spatial grid step	nm	31.25
time step	s	5.0×10^{-12}

Appendix B

Mathematical derivations

B.1 RP check

The new Rayleigh-Plesset equation

$$P_g - P_\infty = \ddot{R}_i \left[\frac{R_i^2}{R_e}(\rho_w - \rho_o) + \rho_o R_i \right] + \dot{R}_i^2 Ri \left[\rho_o \left(\frac{3}{2R_i} - \frac{2}{R_e} + \frac{1}{2}\frac{R_i^3}{R_e^4} \right) + \frac{\rho_w}{R_e}\left(2 - \frac{1}{2}\frac{R_i^3}{R_e^3} \right) \right] + 4\mu_o \left[\frac{\dot{R}_i}{R_i} - \frac{\dot{R}_i R_i^2}{R_e^3} \right] + 4\frac{\dot{R}_i R_i^2}{R_e^3}\mu_w + \frac{2\sigma_{ow}}{R_e} + \frac{2\sigma_o}{R_i} \tag{B.1}$$

Rewriting choosing $\rho_o = \rho_w$, $\mu_o = \mu_w$, $\sigma_{ow} = 0$ and $\sigma_o = \sigma_w$.

$$\begin{aligned} P_g - P_\infty = {} & \ddot{R}_i \left[\frac{R_i^2}{R_e}(\rho_w - \rho_w) + \rho_w R_i \right] \\ & + \dot{R}_i^2 R_i \left[\rho_w \left(\frac{3}{2R_i} - \frac{2}{R_e} + \frac{1}{2}\frac{R_i^3}{R_e^4} \right) + \frac{\rho_w}{R_e}\left(2 - \frac{1}{2}\frac{R_i^3}{R_e^3} \right) \right] \\ & + 4\mu_w \left[\frac{\dot{R}_i}{R_i} - \frac{\dot{R}_i R_i^2}{R_e^3} \right] + 4\frac{\dot{R}_i R_i^2}{R_e^3}\mu_w + \frac{2 \cdot 0}{R_e} + \frac{2\sigma_w}{R_i} \end{aligned} \tag{B.2}$$

Removing terms that cancel

$$P_g - P_\infty = \ddot{R}_i \left[\rho_w R_i \right] + \dot{R}_i^2 R_i \left[\rho_w \left(\frac{3}{2R_i} \right) \right] + 4\mu_w \left[\frac{\dot{R}_i}{R_i} \right] + \frac{2\sigma_w}{R_i}$$

Which can be rewritten to

$$P_g - P_\infty = \rho_w \left(\ddot{R}_i Ri + \frac{3}{2}\dot{R}_i^2 \right) + 4\mu_w \frac{\dot{R}_i}{R_i} + \frac{2\sigma_w}{R_i}$$

Which is the Rayleigh-Plesset equation for a bubble with only one liquid around.

B.2 Ideal gas law, constant in time

The ideal gas law is

$$PV = \frac{m}{\tilde{\mu}} R_g T$$

where P is pressure, V is volume, m is mass, $\tilde{\mu}$ is the molar mass in kilograms per mole, R_g is the ideal gas constant. The simulation is defined such that the mass in each grid-volume remains constant in time. We therefore know that:

$$\frac{PV}{T} = \text{constant}(t) \tag{B.3}$$

Which is also valid for each individual grid volume in the bubble. As mentioned before, the speed of the bubble wall $\dot{R}$ is much smaller than the speed of sound. Therefore the pressure in the bubble is considered homogeneous.

$$\frac{PV_k}{T_k} = \text{constant}(t) \rightarrow P \sum_0^{R_i} \frac{V_k}{T_k} = \text{constant}(t)$$

$$\rightarrow P \sum \frac{V_k}{T_k} = P_0 \frac{V_0}{T_0} = \frac{P_0}{T_0} \frac{4}{3} \pi R_0^3$$

Where subscript 0 stands for the initial value before the laser is turned on. Rewriting this gives

$$P = \frac{P_0}{T_0} \frac{4}{3} \pi R_0^3 \frac{1}{\sum V_k / T_k}$$

where $\sum V_k/T_k$ can be defined as

$$\sum \frac{V_k}{T_k} = \sum \frac{4}{3} \pi \frac{(r_{k-1} + p_k)^3 - r_{k-1}^3}{T_k}$$

B.3 Ideal gas law, constant in radius

Gas regime

As mentioned before, the pressure is constant with respect to the radius inside the bubble. This tells us

$$\frac{V_k}{m_k T_k} = \text{constant}(r)$$

Further rewriting and using that m_k is constant in time, gives

$$\frac{V_k}{T_k} \frac{1}{\rho_0 V_{0k}} = \frac{1}{\rho_0 T_k} \frac{V_k}{V_{0k}} = \frac{1}{\rho_0 T_k} \frac{r_k^3 - r_{k-1}^3}{(k p_0)^3 - ((k-1) p_0)^3} = \frac{R_g}{\tilde{\mu} P}$$

$$r_k^3 - r_{k-1}^3 = \frac{R_g}{\tilde{\mu}P}\rho_0 T_k \left[(kp_0)^3 - ((k-1)\,p_0)^3 \right]$$

$$r_{k-1} = \left(-\frac{R_g}{\tilde{\mu}P}\rho_0 T_k \left[(kp_0)^3 - ((k-1)\,p_0)^3 \right] + r_k^3 \right)^{1/3}$$

Because letting Matlab or Fortran calculate a cubic root takes a long time, an approximation of this equation is used. Rewriting the previous equation gives

$$r_{k-1} = \left(-\frac{R_g}{\tilde{\mu}P}\rho_0 T_k \frac{{r_k}^3}{{r_k}^3} \left[(kp_0)^3 - ((k-1)\,p_0)^3 \right] + r_k^3 \right)^{1/3}$$

$$r_{k-1} = r_k \left(-\frac{R_g}{\tilde{\mu}P}\rho_0 T_k \frac{1}{{r_k}^3} \left[(kp_0)^3 - ((k-1)\,p_0)^3 \right] + 1 \right)^{1/3}$$

We now assume 1 is much bigger than the other term, which makes sens because r_k and r_{k-1} should be almost the same in most cases, a Taylor expansion can be made for $(1-x)^{1/3}$ with x around zero. This gives

$$r_{k-1} = r_k \left(1 + \frac{1}{3}H - \frac{1}{9}H^2 + \frac{10}{162}H^3 \right)$$

with

$$H = -\frac{R_g}{\tilde{\mu}P}\rho_0 T_k \frac{1}{{r_k}^3} \left[(kp_0)^3 - ((k-1)\,p_0)^3 \right] \tag{B.4}$$

B.4 The heat equation

The basic heat equation

$$D\nabla^2 T + \frac{I}{\rho c_p} = \frac{DT}{Dt}$$

Where I is in Wm^{-3}. Since the simulation calculates the temperature for each grid point, and the grid points move along with the movement of mass, the total derivative becomes a normal partial derivative. Furthermore, the simulation is only in the r direction making the heat equation:

$$D\frac{1}{r^2}\frac{\partial}{\partial r}\left(r^2 \frac{\partial T}{\partial r} \right) + \frac{I}{\rho c_p} = \frac{\partial T}{\partial t} \tag{B.5}$$

The second derivative of the temperature with respect to the radius can be approximated with a forward finite difference scheme.

$$\frac{1}{r^2}\frac{\partial}{\partial r}\left(r^2 \frac{\partial T}{\partial r} \right) = \frac{1}{r^2}\frac{\partial}{\partial r}\left(r^2 \frac{T_{k+1} - T_k}{p_{k+1}} \right) = \frac{1}{r_k^2}\frac{\partial}{\partial r}\left((r_k + \frac{1}{2}p_{k+1})^2 \frac{T_{k+1} - T_k}{p_{k+1}} \right)$$

Approximating even further gives a second order central difference scheme.

$$\frac{\partial^2 T}{\partial r^2} = \frac{1}{r_k^2}\left[\frac{\left((r_k + \frac{1}{2}p_{k+1})^2 \frac{T_{k+1}-T_k}{p_{k+1}}\right) - \left((r_{k-1}+\frac{1}{2}p_k)^2\frac{T_k - T_{k-1}}{p_k}\right)}{\frac{1}{2}p_k + \frac{1}{2}p_{k+1}}\right]$$

The derivative of the temperature with respect to time can be given by

$$\frac{\partial T}{\partial t} = \frac{T_k^{n+1} - T_k^n}{dt}$$

The full heat equation now becomes

$$\begin{aligned}\frac{D}{r_k^2}\left[\frac{\left((r_k + \frac{1}{2}p_{k+1})^2 \frac{T_{k+1}-T_k}{p_{k+1}}\right) - \left((r_{k-1}+\frac{1}{2}p_k)^2\frac{T_k - T_{k-1}}{p_k}\right)}{\frac{1}{2}p_k + \frac{1}{2}p_{k+1}}\right]& \\ + \frac{I}{\rho c_p} = \frac{T_k^{n+1} - T_k^n}{dt}& \end{aligned} \tag{B.6}$$

This can be rearranged

$$\begin{aligned}T_k^{n+1} = \frac{dtD}{r_k^2}\left[\frac{\left((r_k + \frac{1}{2}p_{k+1})^2 \frac{T_{k+1}-T_k}{p_{k+1}}\right) - \left((r_{k-1}+\frac{1}{2}p_k)^2\frac{T_k - T_{k-1}}{p_k}\right)}{\frac{1}{2}p_k + \frac{1}{2}p_{k+1}}\right]& \\ + \frac{dtI}{\rho c_p} + T_k^n& \end{aligned} \tag{B.7}$$

Result

The new temperature at a grid point k in terms of the old temperature in the grid points $k-1$, k, $k+1$

$$\begin{aligned}T_k^{n+1} = T_{k-1}^n &\left[\frac{dtD}{r_k^2}\frac{\left(r_{k-1} + \frac{1}{2}p_k)\right)^2}{p_k\left(\frac{1}{2}p_k + \frac{1}{2}p_{k+1}\right)}\right] \\ +T_k^n &\left[1 - \frac{dtD}{r_k^2\left(\frac{1}{2}p_k + \frac{1}{2}p_{k+1}\right)}\left(\frac{\left(r_k + \frac{1}{2}p_{k+1})\right)^2}{p_{k+1}} + \frac{\left(r_{k-1} + \frac{1}{2}p_k)\right)^2}{p_k}\right)\right] \\ +T_{k+1}^n &\left[\frac{dtD}{r_k^2\left(\frac{1}{2}p_k + \frac{1}{2}p_{k+1}\right)}\frac{\left(r_k + \frac{1}{2}p_{k+1})\right)^2}{p_{k+1}}\right] \\ &+\frac{dtI}{\rho c_p}\end{aligned}$$

B.5 Right side of an interface

First we look at the right side of an interface for which grid point values greater or equal to k are known. Just like in the heat equation for the bulk, we want to express the new temperature T_k^{n+1} in terms of the old temperature on three grid points T_k^n,$T_{k\ 1}^n$ and T_{k+2}^n.

$$T_k = T_k \tag{a}$$

Using a Taylor expansion up to second order to get enough precision

$$T_{k+1} = T_k + p_{k+1} T_k' + \frac{p_{k+1}^2}{2} T_k'' \tag{b}$$

$$T_{k+2} = T_k + \left(p_{k+1} + p_{k+2}\right) T_k' + \frac{\left(p_{k+1} + p_{k+2}\right)^2}{2} T_k'' \tag{c}$$

The heat flux across the oil water interface must be conserved leading to the following condition:

$$\lambda_o \frac{\partial T_o}{\partial r}|_{R_e} = \lambda_w \frac{\partial T_w}{\partial r}|_{R_e}$$

We therefore need to know the derivative of the temperature with respect to the radius. To find this we look for $T_k' = A \cdot a + B \cdot b + C \cdot c$ with the capital letters being coefficients and the small letters being the equations presented above, i.e. $T_k' = A \cdot T_k + B \cdot T_{k+1} + C \cdot T_{k+2}$. For this expression we want T_k to be zero which gives

$$A + B + C = 0$$

T_k' should be one giving

$$p_{k+1} \cdot B + \left(p_{k+1} + p_{k+2}\right) \cdot C = 1$$

And T_k'' should be zero giving

$$\frac{p_{k+1}^2}{2} \cdot B + \frac{\left(p_{k+1} + p_{k+2}\right)^2}{2} \cdot C = 0$$

solving this:

$$\frac{p_{k+1}^2}{2} \cdot B = -\frac{\left(p_{k+1} + p_{k+2}\right)^2}{2} \cdot C$$

$$B = -\frac{\left(p_{k+1} + p_{k+2}\right)^2}{p_{k+1}^2} \cdot C$$

and,

$$p_{k+1} \cdot B + \left(p_{k+1} + p_{k+2}\right) \cdot C = 1$$

$$\rightarrow C = \frac{1}{\left(p_{k+1} + p_{k+2}\right) - \frac{\left(p_{k+1} + p_{k+2}\right)^2}{p_{k+1}}}$$

and thus,

$$B = \frac{(p_{k+1} + p_{k+2})}{p_{k+1}p_{k+2}}$$

Now filling in B and C to find A

$$A = -B - C$$

$$A = -\frac{(p_{k+1} + p_{k+2})}{p_{k+1}p_{k+2}} - \frac{1}{(p_{k+1} + p_{k+2}) - \frac{(p_{k+1} + p_{k+2})^2}{p_{k+1}}}$$

More mathematical steps are shown in appendix B.8
Results

$$A = -\frac{(p_{k+1} + p_{k+2})}{p_{k+1}p_{k+2}} - \frac{1}{(p_{k+1} + p_{k+2}) - \frac{(p_{k+1} + p_{k+2})^2}{p_{k+1}}}$$

$$B = \frac{(p_{k+1} + p_{k+2})}{p_{k+1}p_{k+2}}$$

$$C = \frac{1}{(p_{k+1} + p_{k+2}) - \frac{(p_{k+1} + p_{k+2})^2}{p_{k+1}}}$$

to check if this is correct:

To check if these calculations are correct we know the following must be true

$$p_{k+1} \cdot B + (p_{k+1} + p_{k+2}) \cdot C = 1$$

As shown in appendix B.9, this can be rewritten as follows

$$\frac{p_{k+2}}{p_{k+2}} = 1$$

B.6 Left side of an interface

Calculations for the left side of an interface in the full simulation.

$$T_k = T_k \tag{d}$$

$$T_{k-1} = T_k - p_k T_k' + \frac{p_k^2}{2} T_k'' \tag{e}$$

$$T_{k-2} = T_k - (p_k + p_{k-1}) T_k' + \frac{(p_k + p_{k-1})^2}{2} T_k'' \tag{f}$$

$$D + E + F = 0$$

$$-p_k \cdot E - (p_k + p_{k-1}) \cdot F = 1$$

$$\frac{p_k^2}{2} \cdot E + \frac{(p_k + p_{k-1})^2}{2} \cdot F = 0$$

solving this:

$$\frac{p_k^2}{2} \cdot E = -\frac{(p_k + p_{k-1})^2}{2} \cdot F$$

$$E = -\frac{(p_k + p_{k-1})^2}{p_k^2} \cdot F$$

and,

$$-p_k \cdot E - (p_k + p_{k-1}) \cdot F = 1$$

$$\rightarrow F = \frac{1}{\frac{(p_k + p_{k-1})^2}{p_k} - (p_k + p_{k-1})}$$

and thus,

$$E = -\frac{(p_k + p_{k-1})}{p_k p_{k-1}}$$

Using $D = -E - F$ and filling in E and F

$$D = \frac{(p_k + p_{k-1})}{p_k p_{k-1}} - \frac{1}{\frac{(p_k + p_{k-1})^2}{p_k} - (p_k + p_{k-1})}$$

More mathematical steps are shown in appendix B.10

results

$$D = \frac{(p_k + p_{k-1})}{p_k p_{k-1}} - \frac{1}{\frac{(p_k + p_{k-1})^2}{p_k} - (p_k + p_{k-1})}$$

$$E = -\frac{(p_k + p_{k-1})}{p_k p_{k-1}}$$

$$F = \frac{1}{\frac{(p_k + p_{k-1})^2}{p_k} - (p_k + p_{k-1})}$$

B.7 Finding equilibrium temperature as a function of laser power

From (3.16) we know

$$T_{gas,eq} = \frac{-IR_{i,eq}^2}{6\lambda_o} - \frac{(\frac{IR_{i,eq}^3}{3\lambda_o})}{R_{i,eq}} + \frac{(\frac{IR_{i,eq}^3}{3\lambda_o})}{R_{e,eq}}\left(1 - \frac{\lambda_o}{\lambda_w}\right) + \frac{IR_{e,eq}^2}{3\lambda_o}\left(0.5 + \frac{\lambda_o}{\lambda_w}\right) \tag{B.8}$$

$$T_{gas,eq} = \frac{-IR_{i,eq}^2}{6\lambda_o} - \frac{IR_{i,eq}^3}{3\lambda_o R_{i,eq}} + \frac{IR_{i,eq}^3}{3\lambda_o R_{e,eq}}\left(1 - \frac{\lambda_o}{\lambda_w}\right) + \frac{IR_{e,eq}^2}{3\lambda_o}\left(0.5 + \frac{\lambda_o}{\lambda_w}\right) \tag{B.9}$$

$$T_{gas,eq} = \frac{-IR_{i,eq}^2}{6\lambda_o} - \frac{IR_{i,eq}^2}{3\lambda_o} + \frac{IR_{i,eq}^3}{3\lambda_o R_{e,eq}}\left(1 - \frac{\lambda_o}{\lambda_w}\right) + \frac{IR_{e,eq}^2}{3\lambda_o}\left(0.5 + \frac{\lambda_o}{\lambda_w}\right) \tag{B.10}$$

Filling in $R_{e,eq} = (Re0^3 - Ri0^3 + R_{i,eq}^3)^{1/3}$

$$T_{gas,eq} = \frac{-IR_{i,eq}^2}{6\lambda_o} - \frac{IR_{i,eq}^2}{3\lambda_o} + \frac{IR_{i,eq}^3}{3\lambda_o(Re0^3 - Ri0^3 + R_{i,eq}^3)^{1/3}}\left(1 - \frac{\lambda_o}{\lambda_w}\right) + \frac{I(Re0^3 - Ri0^3 + R_{i,eq}^3)^{2/3}}{3\lambda_o}\left(0.5 + \frac{\lambda_o}{\lambda_w}\right) \tag{B.11}$$

From (B.19) we know:

$$\frac{P_0V_0}{T_0} = \frac{PV}{T} \rightarrow T = PV\frac{T_0}{P_0V_0} \tag{B.12}$$

with

$$P = P_\infty + \frac{2\sigma_{go}}{R_{i,eq}} + \frac{2\sigma_{ow}}{R_e}$$

$$P = P_\infty + \frac{2\sigma_{go}}{R_{i,eq}} + \frac{2\sigma_{ow}}{(Re0^3 - Ri0^3 + R_{i,eq}^3)^{1/3}}$$

Filling in B.12

$$T = \left(P_\infty + \frac{2\sigma_{go}}{R_{i,eq}} + \frac{2\sigma_{ow}}{(Re0^3 - Ri0^3 + R_{i,eq}^3)^{1/3}}\right)V\frac{T_0}{P_0V_0} \tag{B.13}$$

Now equating B.11 and B.13 and keeping in mind that **??** is an absolute temperature and B.11 is a relative temperature.

$$\left(P_\infty + \frac{2\sigma_{go}}{R_{i,eq}} + \frac{2\sigma_{ow}}{(Re0^3 - Ri0^3 + R_{i,eq}^3)^{1/3}}\right)V\frac{T_0}{P_0V_0} = \frac{-IR_{i,eq}^2}{6\lambda_o} - \frac{IR_{i,eq}^2}{3\lambda_o} + \frac{IR_{i,eq}^3}{3\lambda_o(Re0^3 - Ri0^3 + R_{i,eq}^3)^{1/3}}\left(1 - \frac{\lambda_o}{\lambda_w}\right) + \frac{I(Re0^3 - Ri0^3 + R_{i,eq}^3)^{2/3}}{3\lambda_o}\left(0.5 + \frac{\lambda_o}{\lambda_w}\right) + T_{room} \tag{B.14}$$

$$\begin{aligned}\left(P_\infty + \frac{2\sigma_{go}}{R_{i,eq}} + \frac{2\sigma_{ow}}{(Re0^3 - Ri0^3 + R_{i,eq}^3)^{1/3}}\right) V \frac{T_0}{P_0 V_0} = \\ \frac{I}{3\lambda_o}[-1.5R_{i,eq}^2 + \frac{R_{i,eq}^3}{(Re0^3 - Ri0^3 + R_{i,eq}^3)^{1/3}}\left(1 - \frac{\lambda_o}{\lambda_w}\right) \\ + (Re0^3 - Ri0^3 + R_{i,eq}^3)^{2/3}\left(0.5 + \frac{\lambda_o}{\lambda_w}\right)] + T_{room}\end{aligned} \tag{B.15}$$

This can be solved to obtain $R_{i,eq}$ as a function of I. However, plotting both sides of the equation in matlab and taking the value where they cross as $R_{i,eq}$ is much easier than actually solving it. When this is done for a bubble with initial inner radius of 3 µm, a triacetin oil layer 1 µm thick and the laser continuously radiating at $10^{10}\,\mathrm{Wm^{-2}}$, an equilibrium radius is found to be 3.0977 µm. In Figure 3.4 it can be seen that the simulation does converge to this value and the predicted temperature profile.

B.8 Math 1

$$p_{k+1} \cdot B + (p_{k+1} + p_{k+2}) \cdot C = 1$$

$$-p_{k+1}\frac{(p_{k+1} + p_{k+2})^2}{p_{k+1}^2} \cdot C + (p_{k+1} + p_{k+2}) \cdot C = 1$$

$$C\left((p_{k+1} + p_{k+2}) - \frac{(p_{k+1} + p_{k+2})^2}{p_{k+1}}\right) = 1$$

$$C = \frac{1}{(p_{k+1} + p_{k+2}) - \frac{(p_{k+1} + p_{k+2})^2}{p_{k+1}}}$$

and thus,

$$B = -\frac{(p_{k+1} + p_{k+2})^2}{p_{k+1}^2} \cdot \frac{1}{(p_{k+1} + p_{k+2}) - \frac{(p_{k+1} + p_{k+2})^2}{p_{k+1}}}$$

$$B = -\frac{(p_{k+1} + p_{k+2})}{p_{k+1}^2} \cdot \frac{1}{1 - \frac{(p_{k+1} + p_{k+2})}{p_{k+1}}}$$

$$B = -\frac{(p_{k+1} + p_{k+2})}{p_{k+1}^2 - p_{k+1}(p_{k+1} + p_{k+2})}$$

$$B = -\frac{(p_{k+1} + p_{k+2})}{p_{k+1}^2 - p_{k+1}^2 - p_{k+1}p_{k+2}}$$

$$B = \frac{(p_{k+1} + p_{k+2})}{p_{k+1}p_{k+2}}$$

$$A = -B - C$$
$$A = -\frac{(p_{k+1} + p_{k+2})}{p_{k+1}p_{k+2}} - \frac{1}{(p_{k+1} + p_{k+2}) - \frac{(p_{k+1} + p_{k+2})^2}{p_{k+1}}}$$

B.9 Math2

$$p_{k+1} \cdot B + (p_{k+1} + p_{k+2}) \cdot C = 1$$

$$p_{k+1} \cdot \frac{(p_{k+1} + p_{k+2})}{p_{k+1}p_{k+2}} + (p_{k+1} + p_{k+2}) \cdot \frac{1}{(p_{k+1} + p_{k+2}) - \frac{(p_{k+1} + p_{k+2})^2}{p_{k+1}}}$$

$$\frac{(p_{k+1} + p_{k+2})}{p_{k+2}} + \frac{1}{1 - \frac{(p_{k+1} + p_{k+2})}{p_{k+1}}}$$

$$\frac{(p_{k+1} + p_{k+2})}{p_{k+2}} + \frac{1}{1 - 1 - \frac{p_{k+2}}{p_{k+1}}}$$

$$\frac{(p_{k+1} + p_{k+2})}{p_{k+2}} - \frac{p_{k+1}}{p_{k+2}}$$

$$\frac{p_{k+1} + p_{k+2} - p_{k+1}}{p_{k+2}}$$

$$\frac{p_{k+2}}{p_{k+2}} = 1$$

B.10 Math3

$$D + E + F = 0$$
$$-p_k \cdot E - (p_k + p_{k-1}) \cdot F = 1$$
$$\frac{p_k^2}{2} \cdot E + \frac{(p_k + p_{k-1})^2}{2} \cdot F = 0$$

solving this:

$$\frac{p_k^2}{2} \cdot E = -\frac{(p_k + p_{k-1})^2}{2} \cdot F$$
$$E = -\frac{(p_k + p_{k-1})^2}{p_k^2} \cdot F$$

and,

$$-p_k \cdot E - (p_k + p_{k-1}) \cdot F = 1$$

$$-p_k \cdot -\frac{(p_k + p_{k-1})^2}{p_k^2} \cdot F - (p_k + p_{k-1}) \cdot F = 1$$

$$F\left(\frac{(p_k + p_{k-1})^2}{p_k} - (p_k + p_{k-1})\right) = 1$$

$$F = \frac{1}{\frac{(p_k + p_{k-1})^2}{p_k} - (p_k + p_{k-1})}$$

and thus,

$$E = -\frac{(p_k + p_{k-1})^2}{p_k^2} \cdot \frac{1}{\frac{(p_k + p_{k-1})^2}{p_k} - (p_k + p_{k-1})}$$

$$E = -\frac{(p_k + p_{k-1})}{p_k^2} \cdot \frac{1}{\frac{(p_k + p_{k-1})}{p_k} - 1}$$

$$E = -\frac{(p_k + p_{k-1})}{p_k\left(p_k + p_{k-1}\right) - p_k^2}$$

$$E = -\frac{(p_k + p_{k-1})}{p_k p_{k-1}}$$

$$D = -E - F$$

$$D = \frac{(p_k + p_{k-1})}{p_k p_{k-1}} - \frac{1}{\frac{(p_k + p_{k-1})^2}{p_k} - (p_k + p_{k-1})}$$

B.11 Static bubble solution

This part is done to examine what the equilibrium temperature is of the bubble with the laser continuously on. When the simulation converges (in the limit) to this temperature it can be concluded the program is correct. This is of course assuming this easy calculation is correct. It starts with the heat equation, taken from (3.13).

$$D\frac{1}{r^2}\frac{\partial}{\partial r}\left(r^2\frac{\partial T}{\partial r}\right) + \frac{I}{\rho c_p} = \frac{DT}{Dt}$$

Normally I (Wm^{-3}) would be a function of time but in this static solution it is taken to be the average laser power. In case the laser is modulated as a sine wave I would be half the maximum laser power. Because we are interested in the unchanging equilibrium case the temperature change in time is zero:

$$D\left(\frac{2}{r}\frac{\partial T}{\partial r}+\frac{\partial^2 T}{\partial r^2}\right)+\frac{I}{\rho c_p}=0$$

An expression for T can be given as a solution to this differential equation

$$T=\frac{-Ir^2}{6c_pD\rho}-\frac{C_1}{r}+C_2$$

Where C_1 and C_2 are constants. The derivatives of this equation are

$$\frac{\partial T}{\partial r}=\frac{-Ir}{3c_pD\rho}+\frac{C_1}{r^2}$$

$$\frac{\partial^2 T}{\partial r^2}=\frac{-I}{3c_pD\rho}-\frac{2C_1}{r^3}$$

By filling the expression for T in the heat equation one can show it is correct:

$$D\left(\frac{2}{r}\left(\frac{-Ir}{3c_pD\rho}+\frac{C_1}{r^2}\right)+\left(\frac{-I}{3c_pD\rho}-\frac{2C_1}{r^3}\right)\right)+\frac{I}{\rho c_p}=0$$

The temperature profile in the different materials:

$$T_{gas}=-\frac{C_{1g}}{r}+C_{2g}$$

Because the thermal diffusivity of the gas is much larger than the thermal diffusivity of water and oil, it is assumed the temperature in the gas is constant with respect to the radius.

$$\frac{\partial T_{gas}}{\partial r}|_0=0\rightarrow C_{1g}=0$$

$$T_{gas}=C_{2g}$$

$$T_{water}=-\frac{C_{1w}}{r}+C_{2w}$$

$$T_{water}|_\infty=0\rightarrow C_{2w}=0$$

$$T_{water}=\frac{-C_{1w}}{r}$$

$$T_{oil}=\frac{-Ir^2}{6c_{po}D_o\rho_o}-\frac{C_{1o}}{r}+C_{2o}$$

with $c_{po}D_o\rho_o=\lambda_o$ and thus

$$T_{oil}=\frac{-Ir^2}{6\lambda_o}-\frac{C_{1o}}{r}+C_{2o}$$

The temperature on both sides of the gas oil interface must be the same:

$$T_{gas} = \frac{-IR_i^2}{6\lambda_o} - \frac{C_{1o}}{R_i} + C_{2o}$$

The temperature on both sides of the oil water interface must be the same:

$$\frac{-C_{1w}}{R_e} = \frac{-IR_e^2}{6\lambda_o} - \frac{C_{1o}}{R_e} + C_{2o}$$

$$C_{1w} = \frac{IR_e^3}{6\lambda_o} + C_{1o} - ReC_{2o}$$

$$T_{water} = \frac{1}{r}\left(\frac{-IR_e^3}{6\lambda_o} - C_{1o} + ReC_{2o}\right)$$

Because the gas has a constant temperature in r, the derivative of the temperature in oil at the interface must be zero:

$$\frac{-IR_i}{3\lambda_o} + \frac{C_{1o}}{R_i^2} = 0 \rightarrow C_{1o} = \frac{IR_i^3}{3\lambda_o}$$

The condition for the boundary between oil and water:

$$\lambda_o \frac{\partial T_o}{\partial r}|_{R_e} = \lambda_w \frac{\partial T_w}{\partial r}|_{R_e}$$

$$\frac{\partial T_o}{\partial r}|_{R_e} = \frac{-IR_e}{3\lambda_o} + \frac{C_{1o}}{R_e^2}$$

$$\frac{\partial T_w}{\partial r}|_{R_e} = \frac{-1}{R_e^2}\left(\frac{-IR_e^3}{6\lambda_o} - C_{1o} + ReC_{2o}\right)$$

$$-\frac{\lambda_o}{\lambda_w}\left(\frac{-IR_e^2}{3\lambda_o} + \frac{C_{1o}}{R_e}\right) + \left(\frac{IR_e^2}{6\lambda_o} + \frac{C_{1o}}{R_e}\right) = C_{2o}$$

$$C_{2o} = \frac{C_{1o}}{R_e}\left(1 - \frac{\lambda_o}{\lambda_w}\right) + \frac{IR_e^2}{3\lambda_o}\left(0.5 + \frac{\lambda_o}{\lambda_w}\right)$$

More mathematical steps can be found in appendix B.12

Results

$$T_{gas,eq} = \frac{-IR_{i,eq}^2}{6\lambda_o} - \frac{C_{1o}}{R_{i,eq}} + C_{2o} \tag{B.16}$$

$$T_{water,eq} = \frac{1}{r}\left(\frac{-IR_{e,eq}^3}{6\lambda_o} - C_{1o} + R_{e,eq}C_{2o}\right) \tag{B.17}$$

$$T_{oil,eq} = \frac{-Ir^2}{6\lambda_o} - \frac{C_{1o}}{r} + C_{2o} \tag{B.18}$$

with

$$C_{1o} = \frac{IR_{i,eq}^3}{3\lambda_o}$$

$$C_{2o} = \frac{C_{1o}}{R_{e,eq}} \left(1 - \frac{\lambda_o}{\lambda_w}\right) + \frac{IR_{e,eq}^2}{3\lambda_o} \left(0.5 + \frac{\lambda_o}{\lambda_w}\right)$$

Subscript eq was added to indicate this is the equilibrium value.

B.12 Math4

The condition for the boundary between oil and water:

$$\lambda_o \frac{\partial T_o}{\partial r}|_{R_e} = \lambda_w \frac{\partial T_w}{\partial r}|_{R_e}$$

$$\frac{\partial T_o}{\partial r}|_{R_e} = \frac{-IR_e}{3\lambda_o} + \frac{C_{1o}}{R_e^2}$$

$$\frac{\partial T_w}{\partial r}|_{R_e} = \frac{-1}{R_e^2} \left(\frac{-IR_e^3}{6\lambda_o} - C_{1o} + ReC_{2o}\right)$$

$$\frac{\partial T_w}{\partial r}|_{R_e} = \frac{IR_e}{6\lambda_o} + \frac{C_{1o}}{R_e^2} - \frac{C_{2o}}{R_e}$$

$$\lambda_o \left(\frac{-IR_e}{3\lambda_o} + \frac{C_{1o}}{R_e^2}\right) = \lambda_w \left(\frac{IR_e}{6\lambda_o} + \frac{C_{1o}}{R_e^2} - \frac{C_{2o}}{R_e}\right)$$

$$\lambda_o \left(\frac{-IR_e}{3\lambda_o} + \frac{C_{1o}}{R_e^2}\right) - \lambda_w \left(\frac{IR_e}{6\lambda_o} + \frac{C_{1o}}{R_e^2} - \frac{C_{2o}}{R_e}\right) = 0$$

$$\lambda_o \left(\frac{-IR_e}{3\lambda_o} + \frac{C_{1o}}{R_e^2}\right) - \lambda_w \left(\frac{IR_e}{6\lambda_o} + \frac{C_{1o}}{R_e^2}\right) = -\frac{\lambda_w C_{2o}}{R_e}$$

$$-\lambda_o \left(\frac{-IR_e}{\lambda_o} + \frac{C_{1o}}{R_e^2}\right) + \lambda_w \left(\frac{IR_e}{6\lambda_o} + \frac{C_{1o}}{R_e^2}\right) = \frac{\lambda_w C_{2o}}{R_e}$$

$$-\frac{\lambda_o}{\lambda_w} \left(\frac{-IR_e}{3\lambda_o} + \frac{C_{1o}}{R_e^2}\right) + \left(\frac{IR_e}{6\lambda_o} + \frac{C_{1o}}{R_e^2}\right) = \frac{C_{2o}}{R_e}$$

$$-\frac{\lambda_o}{\lambda_w} \left(\frac{-IR_e^2}{3\lambda_o} + \frac{C_{1o}}{R_e}\right) + \left(\frac{IR_e^2}{6\lambda_o} + \frac{C_{1o}}{R_e}\right) = C_{2o}$$

$$C_{2o} = \frac{C_{1o}}{R_e} \left(1 - \frac{\lambda_o}{\lambda_w}\right) + \frac{IR_e^2}{3\lambda_o} \left(0.5 + \frac{\lambda_o}{\lambda_w}\right)$$

B.13 Equilibrium radius

Keeping in mind the state equation

$$PV = nR_gT$$

and as we know from (B.3)

$$\frac{P_0V_0}{T_0} = \frac{PV}{T} \to V = \frac{T}{P}\frac{P_0V_0}{T_0} \tag{B.19}$$

p_0, V_0 and T_0 are the initial values from before the laser is turned on. The pressure is the atmospheric pressure plus two Laplace pressures

$$P = P_\infty + \frac{2\sigma_{go}}{R_i} + \frac{2\sigma_{ow}}{R_e}$$

Because we are looking at the static case, T in these equations is the T_{gas} described earlier. Rearranging and filling in gives

$$\frac{4}{3}\pi R_{i,eq}^3 = \frac{T_{gas,eq}P_0V_0}{T_0\left(P_\infty + \dfrac{2\sigma_{go}}{R_{i,eq}} + \dfrac{2\sigma_{ow}}{R_{e,eq}}\right)}$$

and

$$R_{i,eq} = R_{i,0}\left[\frac{T_{gas,eq}P_0}{T_0\left(P_\infty + \dfrac{2\sigma_{go}}{R_{i,eq}} + \dfrac{2\sigma_{ow}}{R_{e,eq}}\right)}\right]^{1/3}$$

B.14 Variations around equilibrium in simplified model

The change in temperature over time can be described as following

$$\left(\rho_oV_{oil}C_{po} + \rho_wV_{w0.1}C_{pw}\right)dT = (B - B_0/2)\cdot V_{oil}dt$$

With ρ_o is the density of the oil, $V_{w0.1}$ is the volume of the first $0.1\,\mu\mathrm{m}$ of water, C_{po} is the heat capacity at constant pressure of the oil, B_0 is the maximum power of the laser and B is the absorbed laser power (Wm^{-3}). In the simulation the laser is modulated as a step function but because all functions can be described by a combination of sine waves a sinusoidal modulation is chosen. This means B becomes a sine function.

$$\frac{dT}{dt} = \frac{(B - B_0/2)\cdot V_{oil}}{\rho_oV_{oil}C_{po} + \rho_wV_{w0.1}C_{pw}} = \frac{B_{amp}\cos(\omega t)\cdot V_{oil}}{\rho_oV_{oil}C_{po} + \rho_wV_{w0.1}C_{pw}} \tag{B.20}$$

$$\to T_g = \frac{B_{amp}\sin(\omega t)\cdot V_{oil}}{\omega\left(\rho_o V_{oil} C_{po} + \rho_w V_{w0.1} C_{pw}\right)} + \text{constant} \tag{B.21}$$

with B_{amp} being the amplitude of the oscillations in the power and $\omega = 2\pi f$. We know that T_g at $t = 0$ and average laser power should be equal to (3.16). Since sin(0) equals zero, the constant is the right part of (3.16). And since this equation is only about a change in temperature, the room temperature should be added.

$$T_g = \frac{B_{amp}\sin(\omega t)\cdot V_{oil}}{\omega\left(\rho_o V_{oil} C_{po} + \rho_w V_{w0.1} C_{pw}\right)} + \frac{-IR_{i,eq}^2}{6\lambda_o} - \frac{C_{1o}}{R_{i,eq}} + C_{2o} + T_{room}$$

I is the average laser power so $B_0/2$ which is the same as B_{amp}. Filling in C_{1o} and C_{2o} and rewriting gives

$$\begin{aligned} T_g = {} & \frac{B_{amp}\sin(\omega t)\cdot V_{oil}}{\omega\left(\rho_o V_{oil} C_{po} + \rho_w V_{w0.1} C_{pw}\right)} \\ & + \frac{-IR_{i,eq}^2}{6\lambda_o} - \frac{IR_{i,eq}^2}{3\lambda_o} + \frac{IR_{i,eq}^3}{3\lambda_o R_{e,eq}}\left(1 - \frac{\lambda_o}{\lambda_w}\right) + \frac{IR_{e,eq}^2}{3\lambda_o}\left(0.5 + \frac{\lambda_o}{\lambda_w}\right) + T_{room} \end{aligned} \tag{B.22}$$

$$\begin{aligned} \to T_g = {} & \frac{B_{amp}\sin(\omega t)\cdot V_{oil}}{\omega\left(\rho_o V_{oil} C_{po} + \rho_w V_{w0.1} C_{pw}\right)} + \\ & \frac{B_{amp}}{3\lambda_o}\left(-1.5R_{i,eq}^2 + \frac{R_{i,eq}^3}{R_{e,eq}}\left(1 - \frac{\lambda_o}{\lambda_w}\right) + R_{e,eq}^2\left(0.5 + \frac{\lambda_o}{\lambda_w}\right)\right) + T_{room} \end{aligned} \tag{B.23}$$

Using equations B.19 we know that

$$P = \frac{P_0 V_0 T_g}{T_0 \frac{4}{3}\pi R_i^3} \tag{B.24}$$

Where T_g can be filled in and P is the total pressure as used in the Rayleigh-Plesset equation (eq 3.10).

The RP equation as seen in (3.10)

$$\begin{aligned} P_g - P_\infty = {} & \ddot{R}_i\left[\frac{R_i^2}{R_e}(\rho_w - \rho_o) + \rho_o R_i\right] + \dot{R}_i^2 R_i\left[\rho_o\left(\frac{3}{2R_i} - \frac{2}{R_e} + \frac{1}{2}\frac{R_i^3}{R_e^4}\right)\right. \\ & \left. + \frac{\rho_w}{R_e}\left(2 - \frac{1}{2}\frac{R_i^3}{R_e^3}\right)\right] + 4\mu_o\left[\frac{\dot{R}_i}{R_i} - \frac{\dot{R}_i R_i^2}{R_e^3}\right] + 4\frac{\dot{R}_i R_i^2}{R_e^3}\mu_w + \frac{2\sigma_{ow}}{R_e} + \frac{2\sigma_o}{R_i} \end{aligned} \tag{B.25}$$

Where P_g is the found P and P_∞ is the pressure at infinity. Expressing this in the new variables P_0 as the pressure at the beginning of the static solution and P_g as the total pressure in the gas, and filling in T_g and the found pressure, this gives:

$$\begin{aligned}
&\frac{P_0 V_0}{T_0 \frac{4}{3}\pi R_i^3} \left[\frac{B_{amp}\sin(\omega t)\cdot V_{oil}}{\omega\left(\rho_o V_{oil} C_{po} + \rho_w V_{w0.1} C_{pw}\right)} \right. \\
&\left. + \frac{B_{amp}}{3\lambda_o}\left(-1.5R_{i,eq}^2 + \frac{R_{i,eq}^3}{R_{e,eq}}\left(1 - \frac{\lambda_o}{\lambda_w}\right) + R_{e,eq}^2\left(0.5 + \frac{\lambda_o}{\lambda_w}\right)\right) + T_{room} \right] \\
&- P_\infty = \ddot{R}_i\left[\frac{R_i^2}{R_e}(\rho_w - \rho_o) + \rho_o R_i\right] + \dot{R}_i^2 R_i \left[\rho_o\left(\frac{3}{2R_i} - \frac{2}{R_e} + \frac{1}{2}\frac{R_i^3}{R_e^4}\right)\right. \\
&\left. + \frac{\rho_w}{R_e}\left(2 - \frac{1}{2}\frac{R_i^3}{R_e^3}\right)\right] + 4\mu_o\left[\frac{\dot{R}_i}{R_i} - \frac{\dot{R}_i R_i^2}{R_e^3}\right] + 4\frac{\dot{R}_i R_i^2}{R_e^3}\mu_w + \frac{2\sigma_{ow}}{R_e} + \frac{2\sigma_o}{R_i}
\end{aligned} \tag{B.26}$$

B.15 Velocity profile

This section shows how the velocity profile used in the simulation is found. It starts with mass conservation:

$$\frac{\partial \rho}{\partial t} + div(\rho v) = 0 \tag{B.27}$$

As mentioned in the chapter, the fluid is considered incompressible and from this we know that

$$0 + \rho div(v) = 0 \rightarrow div(v) = 0 \tag{B.28}$$

We also assume spherical symmetry and the speed is only in the r direction.

$$div(v) = \frac{1}{r2}\frac{\partial}{\partial r}(r^2 v) = 0 \tag{B.29}$$

$$\rightarrow r^2 v = constant(t) \tag{B.30}$$

$$v = \frac{constant}{r^2} \tag{B.31}$$

The speed of the bubble wall is by definition $\dot{R}$ and therefore

$$v(R,t) = \frac{constant}{R^2} = \dot{R} \rightarrow constant(t) = R^2\dot{R} \tag{B.32}$$

$$v(r,t) = \frac{R^2\dot{R}}{r^2} \tag{B.33}$$

Nomenclature

λ	Thermal conductivity ($\mathrm{Wm^{-1}\,K^{-1}}$)
μ	Viscosity
$\overline{\overline{\sigma_o}}$	Strain tensor
$\overrightarrow{e_r}$	Unit vector in the r direction
ρ	Density
σ	Surface tension
σ_{wo}	Interfacial tension between water and oil
$\tilde{\mu}$	Molar mass ($\mathrm{kgmol^{-1}}$)
A	Coefficient to express T_k' at the right side of an interface.
B	Coefficient to express T_k' at the right side of an interface.
B_0	The maximum power of the laser ($\mathrm{Wm^{-3}}$)
B_{amp}	The amplitude of the power of a laser that is sinusoidally modulated ($\mathrm{Wm^{-3}}$)
C	Coefficient to express T_k' at the right side of an interface.
c_p	Heat capacity at constant pressure
D	Coefficient to express T_k' at the left side of an interface.
D	Thermal diffusivity
E	Coefficient to express T_k' at the left side of an interface.
F	Coefficient to express T_k' at the left side of an interface.
f	Laser oscillation frequency
g	Volumic forces e.g. gravity

H	Variable defined in equations B.4 and 3.12
I	Laser power (Wm^{-3})
m	Mass
P	Pressure
P_0	The pressure in the bubble before the laser is turned on
p_0	p_k within the bubble before the laser is turned on
P_∞	The pressure at $r = \infty$, the ambient pressure
p_k	The difference in radius between r_k and r_{k-1}
R	Bubble radius
R_0	Bubble radius (not including the oil) before the laser is turned on
R_e	Bubble radius including the oil layer
R_g	The ideal gas constant
R_i	Bubble radius not including the oil layer
r_k	The radius that belongs to gridpoint k
T	Temperature
t	Time
T_k^n	Temperature at spatial grid point k and temporal grid point n
T_{g2}	The equilibrium absolute gas temperature.
$T_{gas,eq}$	The equilibrium change in gas temperature compared to room temperature.
V	Volume
v	Velocity
subcsript k	Indication of grid number with $k = 1$ being the most inner radius gridpoint.
subscript g	The variable in case of gas
subscript o	The variable in case of oil
subscript w	The variable in case of water

Bibliography

[1] C. Kresser. Thyroid Disorders (????). Retrieved from `http://my.chriskresser.com/ebook/thyroid-disorders` on March 3, 2014.

[2] S. L. Murphy, J. Xu, K. D. Kochanek & V. Statistics. National Vital Statistics Reports Deaths : Final Data for 2010 **61** (2013).

[3] L. Fass. Imaging and cancer: a review. *Molecular oncology* **2**, 115–52 (2008).

[4] S. Mallidi, G. P. Luke & S. Emelianov. Photoacoustic imaging in cancer detection, diagnosis, and treatment guidance. *Trends in biotechnology* **29**, 213–221 (2011).

[5] S. Sirsi & M. Borden. Microbubble compositions, properties and biomedical applications. *Bubble Science, Engineering & ...* **1**, 3–17 (2009).

[6] T. Faez, M. Emmer, K. Kooiman, M. Versluis, A. Van Der Steen & N. De Jong. 20 Years of Ultrasound Contrast Agent Modeling. *IEEE Transactions on Ultrasonics, Ferroelectrics, and Frequency Control* **60**, 7–20 (2013).

[7] G. Lajoinie. *Study of a potential photoacoustic contrast agent, optical heating, bubble formation and high speed cameras.* Master's thesis, University of Twente (2011).

[8] A. G. Bell. On the production and reproduction of sound by light. *American Journal of Science* **Series 3 Vol. 20**, 305–324 (1880).

[9] L. V. Wang & S. Hu. Photoacoustic tomography: in vivo imaging from organelles to organs. *Science (New York, N.Y.)* **335**, 1458–62 (2012).

[10] A. Petschke & P. J. La. Comparison of intensity-modulated continuous-wave lasers with a chirped modulation frequency to pulsed lasers for photoacoustic imaging applications. *Medical and biological imaging* **1**, 1188–1195 (2010).

[11] K. Maslov & L. V. Wang. Photoacoustic imaging of biological tissue with intensity-modulated continuous-wave laser. *Journal of biomedical optics* **13**, 024006 (2008).

[12] R. Gramiak & P. Shah. Echocardiography of the aortic root. *Invest. Radiol* **3**, 356366 (1968).

[13] E. C. Unger, T. Porter, W. Culp, R. Labell, T. Matsunaga & R. Zutshi. Therapeutic applications of lipid-coated microbubbles. *Advanced drug delivery reviews* **56**, 1291–314 (2004).

[14] T. Al-shemmen. *Engineering Fluid Mechanics.* bookboon.com (2012).

[15] P. T. Huynh. Solvent-free beta-carotene nanoparticles for food fortification (2012).

[16] S. Zhang, X. Lu, J. Wu, W. Tong, Q. Lei & W. Fang. Interfacial Tensions for System of *n*-Heptane + Water with Quaternary Ammonium Surfactants and Additives of NaCl or C_2–C_4 Alcohols. *J. Chem. Eng.* **59**, 860–868 (2014).

[17] M. Overvelde. *Ultrasound contrast agents, dynamics of coated bubbles.* Master's thesis, University of Twente (2010).

[18] E. Unger & T. McCreery. Acoustically active lipospheres containing paclitaxel: a new therapeutic ultrasound contrast agent. *Investigative Radiology* **33**, 886–892 (1998).

[19] R. Shih, D. Bardin, T. D. Martz, P. S. Sheeran, P. a. Dayton & A. P. Lee. Flow-focusing regimes for accelerated production of monodisperse drug-loadable microbubbles toward clinical-scale applications. *Lab on a chip* **13**, 4816–26 (2013).

[20] K. Hettiarachchi, A. P. Lee, S. Zhang, S. Feingold & P. a. Dayton. Controllable microfluidic synthesis of multiphase drug-carrying lipospheres for site-targeted therapy. *Biotechnology Progress* **25**, 938–945 (2009).

[21] Y. Gong, M. Cabodi & T. Porter. Relationship between size and frequency dependent attenuation of monodisperse populations of lipid coated microbubbles. *Bubble Science, Engineering & Technology* **2**, 41–47 (2010).

[22] S. a. Peyman, R. H. Abou-Saleh, J. R. McLaughlan, N. Ingram, B. R. G. Johnson, K. Critchley, S. Freear, J. A. Evans, A. F. Markham, P. L. Coletta & S. D. Evans. Expanding 3D geometry for enhanced on-chip microbubble production and single step formation of liposome modified microbubbles. *Lab on a Chip* **12**, 4544 (2012).

[23] M. Kaya, S. Feingold, J. Streeter, K. Hettiarachchi, A. P. Lee & P. a. Dayton. Acoustic characterization of individual monodisperse contrast agents with an optical-acoustical system. *Proceedings - IEEE Ultrasonics Symposium* pp. 1813–1816 (2009).

[24] M. Kaya & S. Feingold. Acoustic responses of monodisperse lipid encapsulated microbubble contrast agents produced by flow focusing. *Bubble Science Engineering Technology* **2**, 33–40 (2010).

[25] K. Hettiarachchi, E. Talu, M. L. Longo, P. a. Dayton & A. P. Lee. On-chip generation of microbubbles as a practical technology for manufacturing contrast agents for ultrasonic imaging. *Lab on a chip* **7**, 463–468 (2007).

[26] E. Talu, K. Hettiarachchi, H. Nguyen, A. P. Lee, R. L. Powell, M. L. Longo & P. a. Dayton. Lipid-stabilized monodisperse microbubbles produced by flow focusing for use as ultrasound contrast agents. *Proceedings - IEEE Ultrasonics Symposium* **1**, 1568–1571 (2006).

[27] E. Talu, K. Hettiarachchi, R. L. Powell, A. P. Lee, P. a. Dayton & M. L.

Longo. Maintaining monodispersity in a microbubble population formed by flow-focusing. *Langmuir* **24**, 1745–1749 (2008).

[28] E. Stride & M. Edirisinghe. Novel microbubble preparation technologies. *Soft Matter* **4**, 2350 (2008).

[29] M. P. Kok. *Pinched flow fractionation for ultrasound contrast agent enrichment*. Master's thesis, University of Twente (2014).

[30] Jong Wook Hong, K. Hosokawa, T. Fujii, M. Seki & I. Endo. Microfabricated polymer chip for capillary gel electrophoresis. *Biotechnology Progress* **17**, 958–962 (2001).

[31] E. Stride & M. Edirisinghe. Novel preparation techniques for controlling microbubble uniformity: a comparison. *Medical & biological engineering & computing* **47**, 883–92 (2009).

[32] E. Talu, K. Hettiarachchi, S. Zhao, R. L. Powell, A. P. Lee, L. Longo & P. A. Dayton. Tailoring the Size Distribution of Ultrasound Contrast Agents: Possible Method for Improving Sensitivity in Molecular Imaging **6**, 384–392 (2007).

Acknowledgements

I would very much like to thank everybody that helped me, collaborated with me or supported me during my work at POF. Some people I would like to thank in particular and above everyone else I would like to thank Guillaume Lajoinie. Having me as a student must be very hard because I had so much to learn. Probably the fact that understanding a French accent was a true challenge for me did not help either. Fortunately, after learning “Quoi de neuf” things got much better. I am sincerely grateful for your efforts in guiding me and I feel like I have learned incredibly much about physics but also how to get things done.

The person that definitely deserves to be mentioned second in line would be Tim Segers. Tim helped me a lot during my project and especially much during my work with microfluidic devices. Technically a great contributor to my results but also the little tips and advice on how to work or write a report helped me a lot.

A very, very, very big thank you goes to Matthijs Neut and Martin Klein Schaarsberg who helped me much more than is good for them. Together they taught me how to use Fortran and they solved many of the computation errors and my confusions with this program and in martins case, also with Latex.

Speaking about simulations, Rodolfo Ostilla Mónico helped me a lot. His advice was always right to the point and very useful. I am really impressed by his skills.

An important step in my project was the arrival of a new Master student that would work on a topic very closely related to an experiment I just started working on. Leonie de Rond and I have collaborated more closely than I have with anyone else which greatly improved my work efficiency and the joy of working. Leonie even deserves a second thank you for helping me find exactly the literature I needed when I needed it.

Also, I would like to thank Wilma Petersen and Klazina Kruizinga for help in the search for the best contrast agents and Pascal Sleutel for effective encouragement. Finally, I would really like to thank Riëlle de Ruiter for saving the day by providing me with the last parameter needed to run my simulations.